Effects of freeplay on the dynamic stability of an aircraft main landing gear

C. Howcroft*, M. Lowenberg†, S. Neild‡

University of Bristol, Bristol, BS8 1TR

B. Krauskopf§

The University of Auckland, Private Bag 92019, Auckland 1142

A study is made into the occurrence of shimmy oscillations in a dual-wheel main landing gear. Nonlinear equations of motion are developed for the system and various effects are considered including gyroscopic coupling, nonlinear tyre properties, geometric nonlinearities and fluid shock damping. Of particular interest in this study is the presence of freeplay — this is introduced as a lateral play at the apex of the torque link joints. Using bifurcation analysis methods, the dynamics of this system are explored as the forward velocity and loading force acting on the gear are varied. For the zero freeplay case the system is found to be stable over its physical operating range with shimmy oscillations appearing only for extreme loading forces and speed. However, with the introduction of freeplay, shimmy may be observed over more typical operating conditions and the resulting oscillations are found to scale linearly with freeplay magnitude. The parameter plane of forward velocity and loading force is then further subdivided into areas of different types of dynamics. With the inclusion of freeplay we observe the appearance of low-frequency and high-frequency shimmy oscillations, bi-stable behaviour and stationary solutions of non-zero yaw. Considering the desirable case where no shimmy occurs we define the set of allowable freeplay profiles that satisfy a conservative stability criteria.

*Department of Engineering Mathematics, University of Bristol, UK (c.howcroft@bristol.ac.uk)
†Department of Aerospace Engineering, University of Bristol, UK (m.lowenberg@bristol.ac.uk)
‡Department of Mechanical Engineering, University of Bristol, UK (simon.neild@bristol.ac.uk)
§Department of Mathematics, University of Auckland, New Zealand (b.krauskopf@auckland.ac.nz)

I. Introduction

Self-sustained oscillations may appear in the dynamics of a wide variety of rolling systems. These oscillations — termed shimmy — are the result of the transfer of energy to the oscillatory degrees of freedom (DoFs) of the system, via the interaction between wheel and ground. This is generally a highly nonlinear phenomenon and, as such, may be very hard to predict, as it only appears under specific circumstances. Shimmy oscillations may occur in the landing gear of civil aircraft.[1] Past studies have successfully applied nonlinear analysis methods for determining the characteristics of this type of oscillation and the parameter ranges over which they occur for a nose landing gear (NLG).[2] Our focus here is on main landing gear (MLG) shimmy.[3] In a previous study[4] we used a nonlinear model with three DoFs to express the dynamics of a MLG of dual-wheel configuration, using numerical continuation methods to study the onset of shimmy oscillations. This model allowed for a single side-stay of arbitrary orientation and we found its positioning to be highly influential on the complexity of the behaviour observed, owing to additional geometric coupling between the different oscillatory DoFs. In this work we extend this model to allow for the presence of mechanical freeplay. Such mechanical freeplay — usually torsional in nature — has long been regarded as an important mechanism in the appearance of shimmy oscillations, and there are a number of studies in the literature concerning its role in their development. Considerations of possible freeplay are particularly important to the long term feasibility of an aircraft landing gear design, as it often develops within the mechanical joints of a landing gear over its service life.

Sura and Suryanarayan[5] point out that freeplay may appear from a multitude of sources including lateral play in the steering collar, the wheel axle, freeplay in the steering system, the fuselage attachment points and the interlinkages of the torque links. Their study considers a nonlinear model of a typical aircraft nose landing gear with freeplay in the steering DoF. By numerical simulation they find that with the introduction of freeplay the amplitude of shimmy oscillations increases and there is a reduction in the critical velocity at which they develop. Similar conclusions are also drawn by Sateesh and Maiti[6] through the analysis of a nonlinear NLG model with torque link freeplay; moreover, the effect of a magneto-rheological damper is investigated and shown to improve the critical shimmy velocity of the system. Woerner and Noel[7] consider shimmy of a dual-wheel MLG system incorporating a multitude of nonlinear effects, including torsional freeplay, nonlinear viscous damping and Coulomb friction. Here, freeplay and friction are both found to have significant effects on the development of shimmy oscillations.

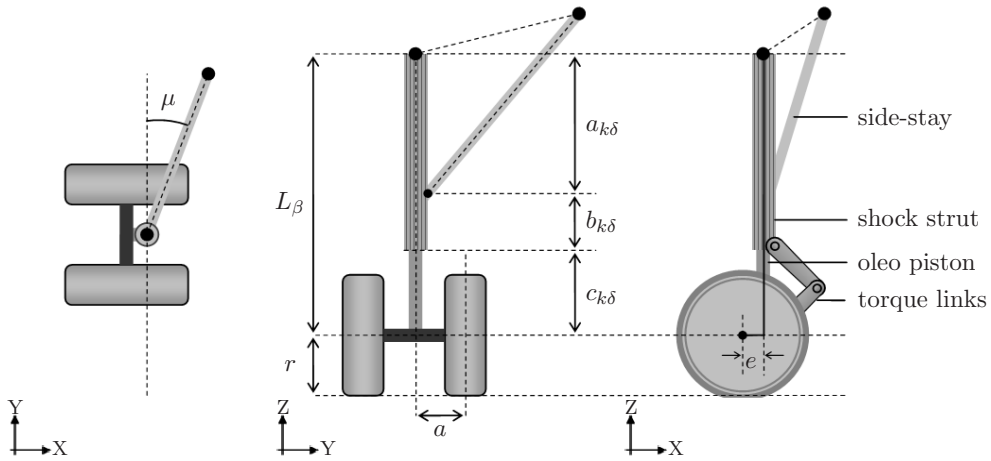

Figure 1. Parameterisation of dual-wheel main landing gear geometry, shown with zero rake angle ϕ.

The MLG model of our previous work[4] is also extended to include an additional axial degree of freedom representing the telescopic compression of the landing gear under load. This compression has a number of effects on the dynamics of the system — particularly regarding the dynamics of the tyres — but is also required to correctly model the appearance of mechanical freeplay in the torque links. In section II we present this extended model, which also includes gyroscopic coupling of the spinning wheel and brake assembly (see §II.B.6) and the variation of system parameters with axial deflection (§II.A) and dynamic loading force (§II.B). In section III we introduce freeplay to the system, and discuss the validity of smooth and non-smooth representations of its characteristics. In section IV we use bifurcation analysis techniques to perform a sensitivity study into the presence of this freeplay and its effects on the shimmy stability of the MLG. Results and conclusions of this work are then presented in section V, where we also point to directions in which this research may be extended further.

II. Four degree-of-freedom dual-wheel MLG model

We consider here a dual-wheel aircraft MLG as shown in figure 1, consisting of a main strut with upper (shock strut) and lower (oleo piston) parts, allowing for telescopic extension and compression of the gear. These upper and lower parts are connected via a pair of torque links that permit this telescopic motion but resist twisting of the MLG; they are discussed in detail in section III. At the base of the gear sits the axle assembly providing a mounting point for the brakes and wheels, which are able to rotate independently. A single side-stay locks the system in place; it is attached both at the aircraft wing and the shock strut. The MLG is also attached to the aircraft at a hinged point at the top of the shock strut. To aid with the definition of geometric parameters we introduce the global axis system (X,Y,Z) with

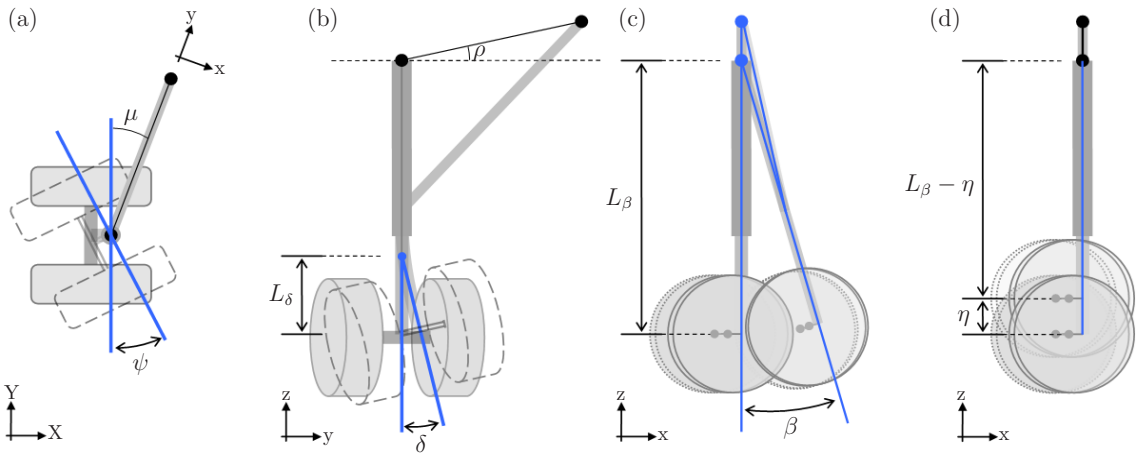

Figure 2. The torsional ψ (a), lateral δ (b), longitudinal β (c) and axial η (d) DoFs used to express the MLG dynamics. Local coordinates (x, y, z) are defined with z aligned with the main strut, x perpendicular to the main strut and side-stay, and y chosen to complete the right-handed coordinate system. For the zero rake angle case shown here z = Z.

X aligned in the forward velocity direction, Z pointing vertically upwards and Y, pointing to the left to complete the right-hand set of coordinates.

We express the dynamics of the MLG system in terms of several oscillatory degrees of freedom, aligned with the side-stay orientation; these are shown in figure 2. In addition to the torsional, lateral and longitudinal motion allowed previously[4] and expressed by the angles ψ, δ and β, we extend our model to include compression of the main strut. This motion is represented by the addition of an axial degree of freedom expressed by the variable η. We note that the inclusion of this axial motion has a number of effects on the MLG system, changing not only the physical length of the gear but also resulting in substantial variation in the loading force acting through the main strut. This results in a large number of parameters — particularly those associated with the tyre dynamics — changing dynamically with variations in η. The dependencies between these parameters (previously fixed[4]) and the additional axial degree of freedom are discussed in more detail in sections II.A – II.B. By considering the motion of the MLG system in terms of the angles ψ, δ, β and η, as well as two additional degrees of freedom λ_L and λ_R describing the lateral deflection of the left and right tyres[4,8] we write the mathematical model of the MLG system as the set of equations:

$$I_\psi\ddot{\psi} + I_a(\dot{\delta}\sin\theta_a + \dot{\beta}\cos\theta_a\cos p)(\dot{\delta}\cos\theta_a - \dot{\beta}\sin\theta_a\cos p) + M_{c\psi} + M_{k\psi} = M_\psi(\mathbf{q}\,,\dot{\mathbf{q}})\,, \tag{1}$$

$$I_\delta\ddot{\delta} - I_a(\dot{\beta}(2\cos^2\theta_a - 1)\cos p + 2\dot{\delta}\sin\theta_a\cos\theta_a)\dot{\theta}_a + \frac{\mathrm{d}I_\delta}{\mathrm{d}\eta}\dot{\eta}\dot{\delta} + c_\delta\dot{\delta} + k_\delta\delta = M_\delta(\mathbf{q}\,,\dot{\mathbf{q}})\,, \tag{2}$$

$$
\begin{aligned}
I_\beta\ddot{\beta} + I_a(\dot{\delta}\sin\theta_s + \dot{\beta}\cos\theta_a\cos p)(\dot{\delta}\cos\theta_a - \dot{\beta}\sin\theta_a\cos p)\sin p \\
-I_a(\dot{\delta}(2\cos^2\theta_a - 1) - 2\dot{\beta}\sin\theta_a\cos\theta_a\cos p)\dot{\theta}_a \\
+M\ddot{H}L_\beta(-H_1\sin\beta + H_2\cos\beta) \\
+\frac{\mathrm{d}I_\beta}{\mathrm{d}\eta}\dot{\eta}\dot{\beta} + (c_\beta\dot{\beta} + M_{c\psi}\sin p) + (k_\beta\beta + M_{k\psi}\sin p) = M_\beta(\mathbf{q}\,,\dot{\mathbf{q}})\,, \qquad (3)
\end{aligned}
$$

$$
-M\ddot{H}\cos\phi - \frac{1}{2}\frac{\mathrm{d}I_\beta}{\mathrm{d}\eta}\dot{\beta}^2 - \frac{1}{2}\frac{\mathrm{d}I_\delta}{\mathrm{d}\eta}\dot{\delta}^2 + F_{c\eta} + F_{k\eta} = F_z\cos\phi\,, \qquad (4)
$$

$$
\dot{\lambda}_L + (\mathbf{V}_{LCF}\cdot\mathbf{u}_f)\lambda_L/L_L + (\mathbf{V}^*_{LCF}\cdot\mathbf{u}_\lambda) = 0\,, \qquad (5)
$$

$$
\dot{\lambda}_R + (\mathbf{V}_{RCF}\cdot\mathbf{u}_f)\lambda_R/L_R + (\mathbf{V}^*_{RCF}\cdot\mathbf{u}_\lambda) = 0\,, \qquad (6)
$$

where

$$
\begin{aligned}
\theta_a &= \psi + \beta\sin p + m \qquad \mathbf{q} = [\,\psi, \delta, \beta, \eta, \lambda_L, \lambda_R\,]\,, \\
\ddot{H} &= (-H_1\sin\beta + H_2\cos\beta)(L_\beta\ddot{\beta} - 2\dot{\eta}\dot{\beta}) + (-H_1\cos\beta - H_2\sin\beta)L_\beta\dot{\beta}^2 - \ddot{\eta}\cos\phi\,, \\
\cos\phi &= H_1\cos\beta + H_2\sin\beta + H_3\,, \\
H_1 &= \cos\phi_0\cos^2\rho + \sin\phi_0\sin\rho\cos\rho\sin\mu\,, \\
H_2 &= -\sin\phi_0\cos\rho\cos\mu\,, \\
H_3 &= \cos\phi_0\sin^2\rho - \sin\phi_0\sin\rho\cos\rho\sin\mu\,, \\
\mathbf{V}_{iCF} &= \mathbf{u}_\psi\times(\mathbf{P}_{iCF} - \mathbf{P}_0)\dot{\psi} + \mathbf{u}_\delta\times(\mathbf{P}_{iCF} - \mathbf{P}_\delta)\dot{\delta} + \mathbf{u}_\beta\times(\mathbf{P}_{iCF} - \mathbf{P}_\beta)\dot{\beta} + \mathbf{u}_\eta\dot{\eta} + \mathbf{e}_X V\,, \\
\mathbf{V}^*_{iCF} &= \mathbf{u}_\delta\times(\mathbf{P}_{iCF} - \mathbf{P}_\delta)\dot{\delta} + \mathbf{u}_\beta\times(\mathbf{P}_{iCF} - \mathbf{P}_\beta)\dot{\beta} + \mathbf{u}_\eta\dot{\eta} + \mathbf{e}_X V\,. \qquad i\in\{L,R\}
\end{aligned}
$$

In particular equation (4) describes the new vertical dynamics of the main landing gear. This vertical variation of the landing gear cannot be neglected in light of the inclusion of the axial degree of freedom η, and the effects of axial acceleration enter the system through the terms $\ddot{H}$, where $H = L_\beta(\eta)\,\cos\phi\,$.

Here, the parameters I_ψ, I_δ, I_β, M are the inertial coefficients of the torsional, lateral, longitudinal and axial DoFs, respectively (M corresponding to the modal mass associated with vertical motion of the MLG); I_a is the roll inertia of the wheels/axle assembly; H is the vertical distance between the top and bottom of the main strut; c_δ, c_β, k_δ, k_β are the damping and stiffness coefficients for the lateral and longitudinal DoFs; $M_{c\psi}$, $M_{k\psi}$, $F_{c\eta}$, $F_{k\eta}$ are nonlinear functions giving the damping and stiffness forces acting on the torsional and axial DoFs respectively; $\mathbf{M}_{\psi,\delta,\beta}$ are moments in the torsional, lateral and longitudinal directions (§II.C);

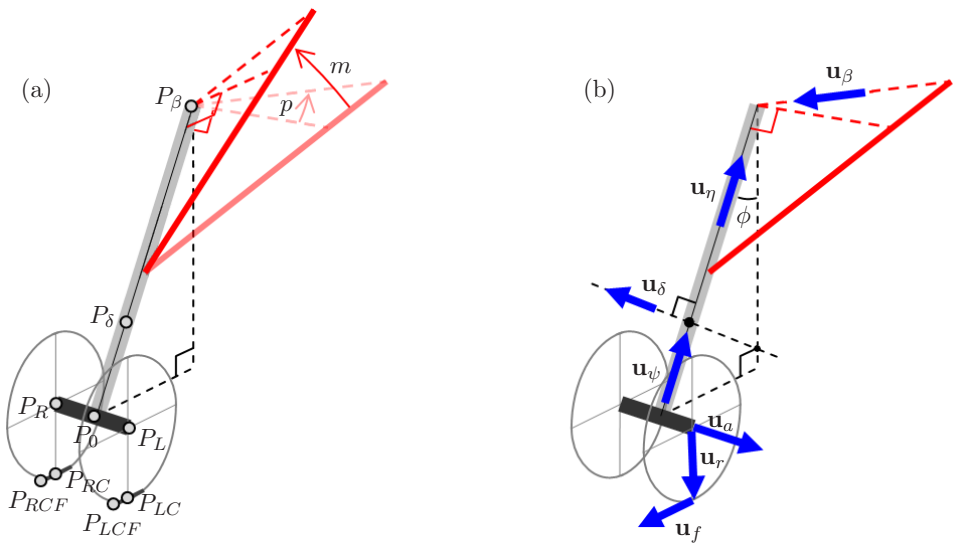

Figure 3. Position (a) and unit (b) vectors used in the derivation of the dual-wheel MLG model. The attachment point orientation is given by the angles m and p where p is applied first; ϕ is the rake angle of the main strut.

V and F_z are the forward velocity and applied loading force, respectively; L_δ is the radius of lateral bending; L_β the gear length; λ_L and λ_R give the lateral deflection of the left and right tyres; $\phi_0 = \phi|_{\beta=0}$ is the initial rake angle; (m, p, μ, ρ) are angular parameters expressing the orientation of the side-stay such that the unit vector $\mathbf{u}_\beta = (-\cos\rho\sin\mu, -\cos\rho\cos\mu, -\sin\rho)$ in the global frame of reference; (m, p) are as shown in figure 3. We note here that throughout the model formulation we use the position and unit vectors $\{\mathbf{P}_{iCF}, \mathbf{P}_0, \mathbf{P}_\delta, \mathbf{P}_\beta, \mathbf{u}_f, \mathbf{u}_\lambda, \mathbf{u}_\psi, \mathbf{u}_\delta, \mathbf{u}_\beta, \mathbf{u}_\eta\}$ to aid in the expression of the MLG geometry and to simplify the resolution of force terms into the oscillatory degrees of freedom. Expressions for these vectors in the global frame of reference are reproduced below from our previous work[4] for completeness of the model; they are also shown graphically in figure 3.

$$\mathbf{P}_\delta = (0,0,0)\,,$$
$$\mathbf{P}_\beta = R(\mathbf{u}_\beta,\beta)R(-\mathbf{e}_Y,\phi_0)(0,0,L_\beta - L_\delta)\,,$$
$$\mathbf{P}_0 = R(\mathbf{u}_\beta,\beta)R(\mathbf{u}_{\delta 0},\delta)R(-\mathbf{e}_Y,\phi_0)(0,0,-L_\delta)\,,$$
$$\mathbf{P}_L = R(\mathbf{u}_\beta,\beta)R(\mathbf{u}_{\delta 0},\delta)R(\mathbf{u}_{\psi 0},\psi_s)R(-\mathbf{e}_Y,\phi_0)(-e,a,-L_\delta)\,,$$
$$\mathbf{P}_R = R(\mathbf{u}_\beta,\beta)R(\mathbf{u}_{\delta 0},\delta)R(\mathbf{u}_{\psi 0},\psi_s)R(-\mathbf{e}_Y,\phi_0)(-e,-a,-L_\delta)\,,$$

$$\mathbf{P}_{LC} = \mathbf{P}_L + (r - d_L)\,\mathbf{u}_r\,,$$
$$\mathbf{P}_{RC} = \mathbf{P}_R + (r - d_R)\,\mathbf{u}_r\,,$$
$$\mathbf{P}_{LCF} = \mathbf{P}_{LC} + 1/2\,h\,\mathbf{u}_f\,,$$
$$\mathbf{P}_{RCF} = \mathbf{P}_{RC} + 1/2\,h\,\mathbf{u}_f\,,$$

$$\mathbf{u}_\beta = \begin{pmatrix} -\cos\rho\sin\mu \\ -\cos\rho\cos\mu \\ -\sin\rho \end{pmatrix}, \quad \mathbf{u}_{\psi 0} = \begin{pmatrix} -\sin\phi_0 \\ 0 \\ \cos\phi_0 \end{pmatrix}, \qquad \mathbf{u}_\eta = R(\mathbf{u}_\beta, \beta) \begin{pmatrix} -\sin\phi_0 \\ 0 \\ \cos\phi_0 \end{pmatrix},$$

$$\mathbf{u}_{\delta 0} = \begin{pmatrix} \cos m\cos\phi_0 \\ -\sin m \\ \cos m\sin\phi_0 \end{pmatrix}, \quad \mathbf{u}_\delta = R(\mathbf{u}_\beta, \beta)\mathbf{u}_{\delta 0}\,, \qquad \mathbf{u}_\psi = R(\mathbf{u}_\beta, \beta)R(\mathbf{u}_{\delta 0}, \delta)\mathbf{u}_{\psi 0}\,,$$

$$\mathbf{u}_\lambda = \frac{1}{|(\mathbf{u}_{a,X}\,, \mathbf{u}_{a,Y}\,, 0)|}(\mathbf{u}_{a,X}\,, \mathbf{u}_{a,Y}\,, 0)\,, \qquad \mathbf{u}_a = R(\mathbf{u}_\beta, \beta)R(\mathbf{u}_{\delta 0}, \delta)R(\mathbf{u}_{\psi 0}, \psi_s)\mathbf{e}_Y\,,$$

$$\mathbf{u}_f = \frac{1}{|(\mathbf{u}_{a,Y}\,, -\mathbf{u}_{a,X}\,, 0)|}(\mathbf{u}_{a,Y}\,, -\mathbf{u}_{a,X}\,, 0)\,, \qquad \mathbf{u}_r = R(\mathbf{u}_f, -\pi/2)\mathbf{u}_a\,.$$

Here the lengths L_β and L_δ are as shown in figure 2; a is half the distance between the left and right wheel centres and $\psi_s = \psi + \beta\sin p$ gives the rotation of the wheel axle relative to the side-stay plane. The notation $R(\mathbf{v}, \theta)$ denotes the rotation matrix corresponding to a rotation of θ radians about the unit vector $\mathbf{v}$.

Equations (5) and (6) express the tyre dynamics of the MLG system, using a stretched-string representation of the tyres. Specifically we employ the von Schlippe approximation[9] of the carcass deflection profile to obtain separate equations for the left and right wheels. These equations are written in terms of the lateral deflection of the forward contact patch points, given by λ_L and λ_R for the left and right wheels, respectively. Here, L_L and L_R denote the relaxation length of each tyre and $\mathbf{e}_\mathrm{X}$, $\mathbf{e}_\mathrm{Y}$, $\mathbf{e}_\mathrm{Z}$ are unit vectors in the global X, Y and Z directions, respectively. We remark that the von Schlippe approximation is not able to capture the pure twisting motion of the tyre contact patch produced by the torsional degree of freedom. This results in a loss of accuracy of the tyre model at lower forward velocities where torsional motion has a greater overall influence on the lateral tyre displacement. To remedy this, we do not allow $\dot{\psi}$ to directly affect the lateral deflection of the contact patch (rather the torsional DoF is able to act on the lateral tyre displacement through secondary effects, e.g. by aligning the lateral tyre vector $\mathbf{u}_\lambda$ with the forward velocity vector); this is achieved through the use of the modified term $\mathbf{V}^*_{iCF}$. This modification has minimal effect on the tyre dynamics at higher forward velocities, but alleviates low-speed inaccuracies such as sustained tyre oscillations at zero velocity. For more information on the implementation of this tyre model we refer to.[4]

Symbol	MLG parameter	Value	Units
Geometric parameters			
ρ	attachment point inclination	0.0	rad
μ	horizontal attachment point orientation	0.0	rad
ϕ_0	initial rake angle	-0.1222	rad (-7°)
e	caster length	0.0	m
a	half track width	0.46	m
l_{tlk}	torque link length	0.35	m
a_{tlk}	upper torque link offset	0.15	m
b_{tlk}	lower torque link offset	0.14	m
r	undeflected tyre radius	0.58	m
Structural parameters			
M	vertical modal mass	3×10^4	kg
I_ψ	torsional inertia	150	kg m^2
I_0	wheel yaw inertia	11	kg m^2
I	wheel polar inertia	19	kg m^2
c_ψ	torsional damping	410	N m s rad^{-1}
c_β	longitudinal damping	3100	N m s rad^{-1}
k_{tlk}	torque link stiffness	3.90×10^7	N m^{-1}
k_β	longitudinal stiffness	1×10^7	N m rad^{-1}
Continuation parameters			
V	forward velocity	0 – 600	m s^{-1}
y_{fp}	torque link freeplay	0 – 2.0	mm
F_z^*	dimensionless loading force	0 – 3.5	–

Table 1. Parameters and their values as used in the analysis of the MLG.

II.A. Effects of Axial DoF

From inspection of the equations of motion (3) and (4) we note that, since the modal mass M is large, the axial DoF will couple strongly with the longitudinal DoF through the $M\ddot{H}$ terms, which both act to produce vertical variation of the attachment points. Axial deflection of the MLG also has a direct effect on certain parameters of the system, such as the gear length and inertia. In this paper we broadly categorise parameters into those that depend explicitly on this axial variation, either directly through the gear length η or through changes in the loading force acting through the gear, and those that do not. Table 1 lists parameter values for the main landing gear model that remain fixed in value and independent of η. Their values — as well as all other parameters throughout this study — are chosen from available industrial data to represent the dual-wheel MLG of a typical mid-sized passenger aircraft. Note that the dimensionless parameter $F_z^* = F_z\,(9.807 \times 3 \times 10^4)^{-1}$ is used to express the loading force acting on the MLG as a proportion of the nominal loading force when the aircraft wings are producing zero lift.

In addition to the values given in Table 1 there are also further parameters in the model representing physical characteristics of the system that are affected directly by the gear compression η. These represent quantities such as gear length and strut stiffness, and their definitions with respect to η are written:

$$
\begin{aligned}
z_{_{tlk}} &= 0.605 - \eta \,, && \text{[m]} \\
L_\beta &= 2.915 - \eta \,, && \text{[m]} \\
L_\delta &= 1.266 - \eta \,, && \text{[m]} \\
I_\beta &= \left(640 L_\beta^2 - 100 L_\beta + 260\right) \cos^2 p \,, && \text{[kg m}^2\text{]} \\
I_\delta &= 630 L_\delta^2 - 140 L_\delta + 60 + I_a \cos^2 \theta_a \,, && \text{[kg m}^2\text{]} \\
k_\delta &= K_{k\delta} L_\delta^2 \left(3 b_{k\delta} c_{k\delta} (b_{k\delta} + c_{k\delta}) + a_{k\delta}(b_{k\delta}^2 + c_{k\delta}^2) + (b_{k\delta}^3 + R_{k\delta} c_{k\delta}^3) + 2 a_{k\delta} b_{k\delta} c_{k\delta}\right)^{-1} , && \text{[N m rad}^{-1}\text{]} \\
c_\delta &= 1.66 \times 10^7 \sqrt{I_\delta k_\delta} \,, && \text{[N m s rad}^{-1}\text{]} \\
F_{k\eta} &= \frac{1}{\pi}\left(a_{k\eta} e^{(b_{k\eta}\eta)} + c_{k\eta}\right)\left[\tan^{-1}(+1 \times 10^5\,(\eta - 0.34)) + \frac{\pi}{2}\right] , \\
&\quad + \frac{1}{\pi}\left(d_{k\eta} e^{(e_{k\eta}\eta)} + f_{k\eta}\right)\left[\tan^{-1}(-1 \times 10^5\,(\eta - 0.34)) + \frac{\pi}{2}\right] - \frac{40}{\eta} \,, && \text{[N]} \\
F_{c\eta} &= \operatorname{sign}(\dot\eta)\left(\frac{4 \times 10^4}{\pi}\tan^{-1}(1 \times 10^4(\eta - 0.18)) + 7.5 \times 10^4\right)\dot\eta^2 + 1000\dot\eta \,, && \text{[N]}
\end{aligned}
$$

$$
\begin{aligned}
&\theta_a = \psi + \beta \sin p + m \qquad I_a = 440 a^2 + 5 + 2 I_0 \\
&a_{k\delta} = 1.649 \quad b_{k\delta} = 0.611 \quad c_{k\delta} = 0.655 - \eta \quad K_{k\delta} = 6.067 \times 10^6 \quad R_{k\delta} = 8/3 \,, \\
&a_{k\eta} = 612.4 \quad b_{k\eta} = 16.72 \quad c_{k\eta} = 2483 \quad d_{k\eta} = 0.3851 \quad e_{k\eta} = 31.39 \quad f_{k\eta} = 1.885 \times 10^5 \,.
\end{aligned}
$$

Here k_δ is the lateral stiffness of the MLG — increasing as the gear is compressed, $2I_0$ is the yaw inertia of the rotating wheels/brakes, and subscripts $_{k\delta}$ and $_{k\eta}$ refer to constants fitted to data for the lateral and axial stiffness functions, respectively. Moreover, c_δ is chosen such that the lateral damping remains a constant proportion of the critical damping over all axial deflections; $F_{k\eta}$ and $F_{c\eta}$ describe the force characteristics of the shock strut assuming a two-stage oleo with fluidic damping. The linear part of $F_{c\eta}$ represents a small correction to the axial damping, required to ensure non-conservatism of the linearised solution about $\eta = 0$. This allows for the identification and continuation of Hopf bifurcation curves in our later analysis.

II.B. Influence of dynamic vertical force

A further consequence of the addition of the axial DoF is that the loading force acting on the MLG changes dynamically with any vertical excitation of the system. Therefore, variation of system parameters that depend explicitly on the applied loading force must be considered when capturing the overall dynamics of the system. In particular, we find that the properties of the pneumatic tyres prove very sensitive in this respect; for example, larger loading forces result in greater tyre inflation pressures influencing multiple aspects of the tyre dynamics.[10] Below we outline extensions to the deflection, effective radius, contact patch, relaxation length and reactive force characteristics of the rolling tyres, which we allow to vary with the applied dynamic load. Since the left and right tyres are assumed to have equal properties, we use the subscript $i \in \{L, R\}$ to refer to parameter definitions that may be applied to either wheel.

II.B.1. Tyre deflection

We split the loading force acting through the landing gear into separate components F_L and F_R acting on the left and right wheels. This is achieved by using a static force balance on the wheel axle, satisfying the expressions

$$\begin{aligned} F_L + F_R &= F_{\text{dyn}} \,, \\ d_L + 2a\varepsilon &= d_R \,, \\ F_{\text{dyn}} &= M\ddot{H} + F_z \,, \qquad i \in L, R \end{aligned}$$

where d_L and d_R are the deflection of the left and right tyres, respectively, and ε is the angle (assumed small) between the wheel axle $\mathbf{u}_a$ and the ground (X, Y)-plane. For each tyre the deflection is related to the applied load by the following quadratic relation fitted to proprietary industrial data:

$$\begin{aligned} d_i &= a_{di}\sqrt{(F_i + b_{di})} - a_{di}\sqrt{b_{di}} \,, \qquad [\text{m}] \\ a_{di} &= 4.221 \times 10^{-4} \,, \\ b_{di} &= 5.107 \times 10^{4} \,. \end{aligned}$$

II.B.2. Effective tyre radius

In the absence of slip, the effective radius r_{eff} of a tyre is related to its angular velocity $\dot{\omega}$ and forward velocity V by

$$r_{\text{eff}}\,\dot{\omega} = V \,.$$

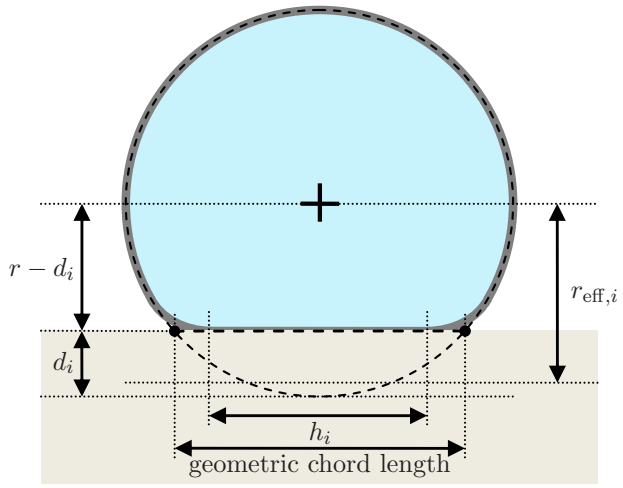

Figure 4. Parameters used to express the deflected geometry of a pneumatic tyre.

Therefore, for a pneumatic tyre subject to a deflection d_i one might expect the effective radius to be equal to the geometric radius of the deflected tyre $r_{\text{eff}} = r - d_i$; see figure 4. However, in general this is not the case and for most tyres the effective radius is larger than this geometric radius. For this study we use the relation for effective radius as suggested by Daugherty,[11]

$$r_{\text{eff},i} = r - \frac{1}{5} d_i \, . \qquad \text{[m]}$$

II.B.3. Contact patch length

In a similar manner to the effective radius, the contact patch length h_i for a deflected pneumatic tyre is not equal to what one would suspect from consideration of a circle of equal radius to the tyre. Rather the contact patch length is typically less than the chord length at distance $r - d_i$ from the wheel centre; see figure 4. Experimental data[12] suggests a contact patch length of 85% of the geometric chord length. Therefore, h_i may be written as

$$h_i = 0.85 \times 4r \sqrt{\left(\frac{d_i}{2r}\right) - \left(\frac{d_i}{2r}\right)^2} \, . \qquad \text{[m]}$$

II.B.4. Relaxation length

The relaxation length is particularly important in determining the delay characteristics of a pneumatic tyre, expressing the distance the tyre must travel to realise the restoring force resulting from a lateral or torsional deformation. This relaxation length usually increases with increasing vertical load. Here we assume that L_L and L_R scale with the contact patch

length.[13] Therefore, based on available tyre data, we use the expression

$$L_i = 0.7 h_i \; . \qquad \text{[m]}$$

II.B.5. Tyre contact forces

The slip angle ($\alpha_i = \tan^{-1}(\lambda_i / L_i)$) given by equations (5) and (6), is used to calculate the cornering force and self-aligning moment produced by each tyre.[4] For this study we use the Pacejka magic tyre formula[14] to give expressions for these reaction forces, which take the following form.

Lateral tyre force:

$$\mathbf{F}_{\mathrm{k}\lambda i} = D_{\mathrm{Fk}\lambda i} \sin\left(C_{\mathrm{Fk}\lambda i} \tan^{-1}(B_{\mathrm{Fk}\lambda i}\alpha - E_{\mathrm{Fk}\lambda i}(B_{\mathrm{Fk}\lambda i}\alpha - \tan^{-1}(B_{\mathrm{Fk}\lambda i}\alpha)))\right) \mathbf{u}_\lambda \; . \qquad (7)$$

Self-aligning moment:

$$\mathbf{M}_{\mathrm{k}\alpha i} = D_{\mathrm{Mk}\alpha i} \sin\left(C_{\mathrm{Mk}\alpha i} \tan^{-1}(B_{\mathrm{Mk}\alpha i}\alpha - E_{\mathrm{Mk}\alpha i}(B_{\mathrm{Mk}\alpha i}\alpha - \tan^{-1}(B_{\mathrm{Mk}\alpha i}\alpha)))\right) \mathbf{e}_Z \; . \qquad (8)$$

Again, these tyre forces depend strongly on loading force. We therefore define the constants in the equations above as functions of F_i. Using tyre data and suggested empirical expressions[15] we write the constants as:

$$C_{\mathrm{Fk}\lambda i} = 1.34 \; ,$$

$$D_{\mathrm{Fk}\lambda i} = a_{1_{\mathrm{Fk}\lambda}} + (a_{2_{\mathrm{Fk}\lambda}} + a_{3_{\mathrm{Fk}\lambda}} F_i)^{0.5} \; ,$$

$$E_{\mathrm{Fk}\lambda i} = a_{6_{\mathrm{Fk}\lambda}} {F_i}^2 + a_{7_{\mathrm{Fk}\lambda}} F_i + 0.95 \; ,$$

$$B_{\mathrm{Fk}\lambda i} = \frac{(a_{4_{\mathrm{Fk}\lambda}} \sin(1.8 \tan^{-1}(F_i / a_{5_{\mathrm{Fk}\lambda}})))}{(C_{\mathrm{Fk}\lambda} D_{\mathrm{Fk}\lambda i})} \; ,$$

$a_{1_{\mathrm{Fk}\lambda}} = -2.828 \times 10^4$, $a_{5_{\mathrm{Fk}\lambda}} = 4.126 \times 10^4$,

$a_{2_{\mathrm{Fk}\lambda}} = 7.9978 \times 10^8$, $a_{6_{\mathrm{Fk}\lambda}} = -1.486 \times 10^{-11}$,

$a_{3_{\mathrm{Fk}\lambda}} = 7.7459 \times 10^4$, $a_{7_{\mathrm{Fk}\lambda}} = -7.036 \times 10^{-6}$,

$a_{4_{\mathrm{Fk}\lambda}} = 6.789 \times 10^5$,

$$C_{\mathrm{Mk}\alpha i} = 3.6\,, \qquad a_{1_{\mathrm{Mk}\alpha}} = 9.524\times10^{-8}, \quad a_{5_{\mathrm{Mk}\alpha}} = -3.1\times10^{-11},$$

$$D_{\mathrm{Mk}\alpha i} = a_{1_{\mathrm{Mk}\alpha}} {F_i}^2 + a_{2_{\mathrm{Mk}\alpha}} F_i\,, \qquad a_{2_{\mathrm{Mk}\alpha}} = 9.364\times10^{-3}, \quad a_{6_{\mathrm{Mk}\alpha}} = 2.34\times10^{-5},$$

$$E_{\mathrm{Mk}\alpha i} = a_{5_{\mathrm{Mk}\alpha}} {F_i}^2 + a_{6_{\mathrm{Mk}\alpha}} F_i + 0.95 + \frac{a_{6_{\mathrm{Mk}\alpha}}^2}{4.0\, a_{5_{\mathrm{Mk}\alpha}}}\,, \quad a_{3_{\mathrm{Mk}\alpha}} = 1.167\times10^{-6},$$

$$B_{\mathrm{Mk}\alpha i} = \frac{(a_{3_{\mathrm{Mk}\alpha}} {F_i}^2 + a_{4_{\mathrm{Mk}\alpha}} F_i)}{(C_{\mathrm{Mk}\alpha} D_{\mathrm{Mk}\alpha i} \exp(10^{-6} F_i))}\,, \qquad a_{4_{\mathrm{Mk}\alpha}} = 1.39\times10^{-1}.$$

II.B.6. Gyroscopic moment

In addition to the forcing terms detailed above we also consider the gyroscopic effect of the spinning wheel/brake assembly[8] and its impact on the dynamics of the MLG system. These gyroscopic moments are indirectly related to the loading force acting through the gear in the sense that a larger loading force results in a smaller effective tyre radius and, therefore, a greater angular velocity of the wheels and brake rotors. We express this gyroscopic coupling in terms of the axle velocity vector $\boldsymbol{\Omega}$ and the wheel spin vector $\boldsymbol{\omega}_i$, writing the gyroscopic moments acting on the system as given by

$$\mathbf{M}_{\mathrm{gyr}_i} = \boldsymbol{\Omega} \times I\boldsymbol{\omega}_i\,, \tag{9}$$

with the vectors

$$\boldsymbol{\Omega} = \dot{\psi}\mathbf{u}_\psi + \dot{\delta}\mathbf{u}_\delta + \dot{\beta}\mathbf{u}_\beta\,, \qquad \boldsymbol{\omega}_i = \frac{(\mathbf{V}_{iCF} \cdot \mathbf{u}_f)}{r_{\mathrm{eff},i}}\mathbf{u}_a\,.$$

Here, I is the axial inertia of the spinning wheels and brake elements, where we assume deflection of the tyres to have a negligible effect on this inertia.

II.C. Forcing terms

For our system the forcing terms M_ψ, M_δ, M_β and F_η derive from the resolution of the lateral tyre forces ($\mathbf{F}_{\mathrm{k}\lambda L}$, $\mathbf{F}_{\mathrm{k}\lambda R}$), self-aligning moments ($\mathbf{M}_{\mathrm{k}\alpha L}$, $\mathbf{M}_{\mathrm{k}\alpha R}$), gyroscopic restoring moment ($\mathbf{M}_{\mathrm{gyr}L}$, $\mathbf{M}_{\mathrm{gyr}R}$) and vertical reaction forces ($\mathbf{F}_L$, $\mathbf{F}_R$), into the four directions $\mathbf{u}_\psi$,

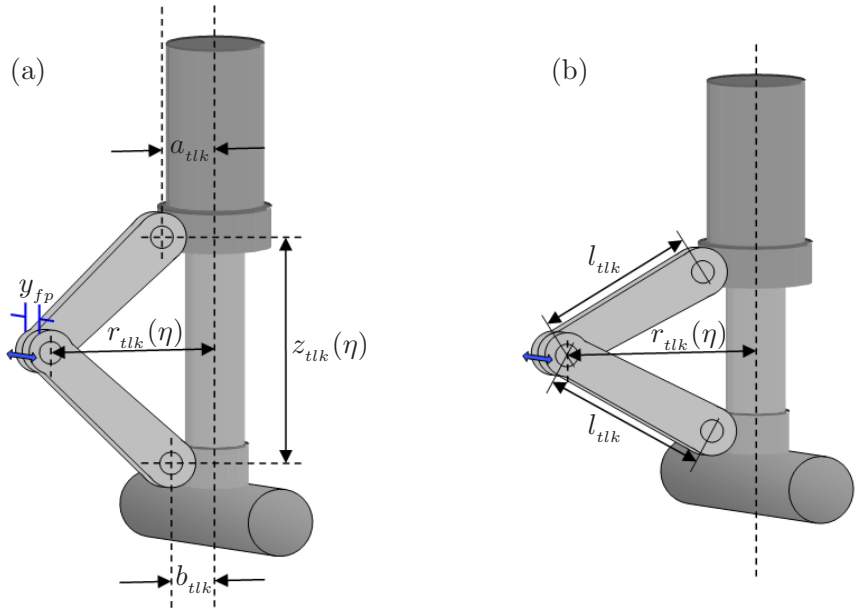

Figure 5. Parameterised representation of the MLG torque link geometry, shown for the zero caster length case $e = 0$. The translational freeplay y_{fp}, introduced at the torque link apex, acts over the radius $r_{tlk}(\eta)$ to produce an angular freeplay in the torsional DoF ψ_{fp}.

$\mathbf{u}_\delta$, $\mathbf{u}_\beta$ and $\mathbf{u}_\eta$. This allows these moment terms to be written as

$$M_\psi = \sum_{i\in\{L,R\}} \left(\left(\mathbf{P}_{iC} - \mathbf{P}_0\right) \times \left(\mathbf{F}_i + \mathbf{F}_{\mathrm{k}\lambda i}\right) - \mathbf{M}_{\mathrm{k}\alpha i} - \mathbf{M}_{\mathrm{gyr}_i} \right) \cdot \mathbf{u}_\psi \ , \tag{10}$$

$$M_\delta = \sum_{i\in\{L,R\}} \left(\left(\mathbf{P}_{iC} - \mathbf{P}_\delta\right) \times \left(\mathbf{F}_i + \mathbf{F}_{\mathrm{k}\lambda i}\right) - \mathbf{M}_{\mathrm{k}\alpha i} - \mathbf{M}_{\mathrm{gyr}_i} \right) \cdot \mathbf{u}_\delta \ , \tag{11}$$

$$M^*_\beta = \sum_{i\in\{L,R\}} \left(\left(\mathbf{P}_{iC} - \mathbf{P}_\beta\right) \times \left(\mathbf{F}_i + \mathbf{F}_{\mathrm{k}\lambda i}\right) - \mathbf{M}_{\mathrm{k}\alpha i} - \mathbf{M}_{\mathrm{gyr}_i} \right) \cdot \mathbf{u}_\beta \ ,$$

$$M_\beta = M^*_\beta - M_\psi(\mathbf{u}_\beta \cdot \mathbf{u}_\psi) \ , \tag{12}$$

$$F_\eta = \sum_{i\in\{L,R\}} \left(\mathbf{F}_i + \mathbf{F}_{\mathrm{k}\lambda i} \right) \cdot \mathbf{u}_\eta \ , \tag{13}$$

with M_β taking a modified form due to geometric coupling between the DoFs ψ and β.

III. Introduction of freeplay

It now remains to define the torsional stiffness and damping functions $M_{k\psi}$ and $M_{c\psi}$, and it is through these terms that we will introduce torsional freeplay to the system. In particular, we consider a freeplay source originating from the torque links of the MLG. These torque links are responsible for preventing the relative rotation between the upper and lower part

of the landing gear whilst still allowing for telescopic extension and retraction of the system; their geometry and placement on the MLG system are shown in figure 5. The freeplay that we consider enters the system at the apex of these torque links, representing a lateral play in the mechanical joint between them. Past studies have found such freeplay to have an important role in the appearance of shimmy oscillations.[5–7,16] From the geometry of the torque links shown in figure 5 we can see that the translational freeplay $y_{_{fp}}$ will result in an angular freeplay $\psi_{_{fp}}$ in the torsional degree of freedom, which is dependent on the distance $r_{_{tlk}}(\eta)$ from the torque link apex to the central strut axis. An important consequence of this is that, as the loading force acting on the landing gear increases and the MLG compresses, this distance changes, resulting in a torsional freeplay that is dependent on the axial DoF. The magnitude of torsional freeplay $\psi_{_{fp}}$ may be written as

$$\begin{aligned}
\psi_{_{fp}} &= y_{_{fp}} r_{_{tlk}} \ , \\
r_{_{tlk}} &= a_{_{tlk}} + l_{_{tlk}} \sin\left(\cos^{-1}\left(\frac{\sqrt{z_{_{tlk}}^2 + (a_{_{tlk}} - b_{_{tlk}})^2}}{2 l_{_{tlk}}} \right) - \tan^{-1}\left(\frac{a_{_{tlk}} - b_{_{tlk}}}{z_{_{tlk}}} \right) \right) \ ,
\end{aligned}$$

where $a_{_{tlk}}$, $b_{_{tlk}}$, $l_{_{tlk}}$, $z_{_{tlk}}$ are constants defining the geometry of the torque link assembly as shown in figure 5.

A similar argument applies to the torsional stiffness of the system whereby we consider a lateral stiffness of the MLG torque links of $k_{_{tlk}}$ acting at a distance $r_{_{tlk}}(\eta)$ from the torsional centre line. For constant $r_{_{tlk}}$ and zero freeplay $\psi_{_{fp}}, y_{_{fp}} = 0$ we model these torque links as a constant linear stiffness between the shock strut and oleo piston. However, this stiffness varies with the introduction of freeplay and axial deflection of the MLG. For this study we assume negligible torsional stiffness while the torque links are not in contact, and initially consider a non-smooth transition to linear stiffness at the boundaries of the freeplay region. This results in the following non-smooth representation of torsional stiffness:

$$M_{k\psi} = \begin{cases} k_{_{tlk}}(y_{_{tlk}} + y_{_{fp}}) r_{_{tlk}} & y_{_{tlk}} < -y_{_{fp}} \\ 0 & |y_{_{tlk}}| < y_{_{fp}} \\ k_{_{tlk}}(y_{_{tlk}} - y_{_{fp}}) r_{_{tlk}} & y_{_{tlk}} > y_{_{fp}} \end{cases} \ , \tag{14}$$

$$\begin{aligned}
y_{_{tlk}} &= r_{_{tlk}} \psi_s \ , \\
\psi_s &= \psi + \beta \sin p \ .
\end{aligned}$$

Whilst this non-smooth model of torque link freeplay gives a simple representation of the contact dynamics over the region of torque link freeplay, we note that in practice the transition between the freeplay and contact regions for a physical system is unlikely to be truly non-smooth. Instead, factors such as the presence of dirt, grease and the degradation and wear of torque link components will all lead to the creation of resistive and dissipative forces within the apex joint. As a result, the true dynamics of the system will differ from the idealised non-smooth case. In particular, this will result in a very rapid transition from zero to non-zero stiffness that will, nonetheless, still occur over a small finite range of $y_{_{fp}}$. To reflect this behaviour we therefore consider the smoothed representation of equation (14), parameterised by the smoothing parameter ϵ as

$$M_{k\psi}(\epsilon) = k_{_{tlk}} \frac{1}{\pi} \left((y_{_{tlk}} + y_{_{fp}}) \left[\tan^{-1} \left(- (y_{_{tlk}} + y_{_{fp}})/\epsilon \right) + \frac{\pi}{2} \right] \right.$$
$$\left. + (y_{_{tlk}} - y_{_{fp}}) \left[\tan^{-1} \left(+ (y_{_{tlk}} - y_{_{fp}})/\epsilon \right) + \frac{\pi}{2} \right] \right) r_{_{tlk}} \ , \qquad (15)$$

Equations 15 approaches the non-smooth case (14) as $\epsilon \to 0$. The solid curves in figure 6 illustrate this approximation for five values of ϵ, where the non-smooth case $M_{k\psi}(0)$ of equation (14) is represented by the dashed line. In particular, we note that ϵ has units of length and visually spans about half of the smoothing region as shown in figure 6(b). The effect of this smoothing is explored in more detail in section IV.D, where we explore the quantitative effect of freeplay magnitude on the dynamics of the system. This is achieved by varying the parameters $y_{_{fp}}$ and ϵ in one of two ways. The first of these is treated in section IV.D.1 wherein ϵ is chosen such that the quantity $(y_{_{fp}}/\epsilon)$ remains constant as torque link freeplay is varied. This ensures that the smoothing region of the freeplay stiffness profile is held as a constant proportion of the freeplay width, hence preserving the shape of the stiffness profile. This is later seen to produce a simple scaling of the shimmy oscillations present in the system; however, this type of freeplay variation is somewhat non-physical with ϵ approaching zero as $y_{_{fp}} \to 0$, tending towards the non-smooth case. A second and more realistic method of scaling is considered in section IV.D.2, where ϵ prescribes a finite smoothing region that is held fixed as torque link freeplay is varied; in a modelling context such a region could correspond to the physical presence of dirt, grease or other material at the torque link apex.

For the torsional damping $M_{c\psi}$ of the system, we assume that damping forces originate largely from viscous dissipation within the shock absorber assembly and energy loss from

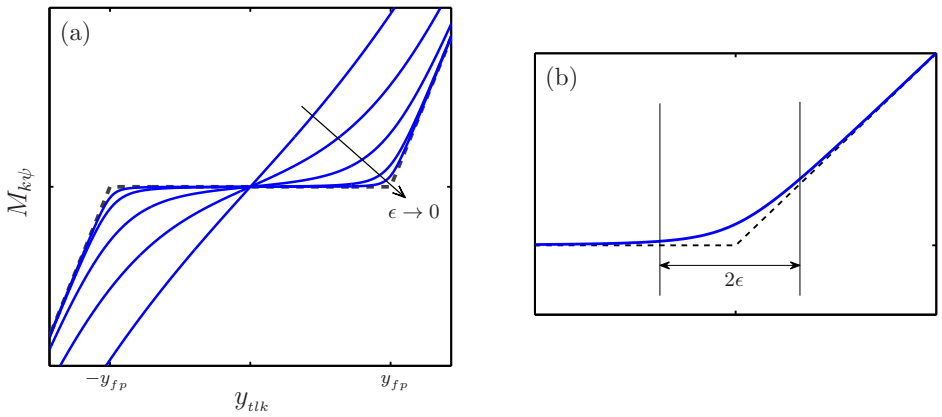

Figure 6. (a) Torsional stiffness profile for $\epsilon = 2y_{fp}$ mm, $\epsilon = y_{fp}$ mm, $\epsilon = 0.5y_{fp}$ mm, $\epsilon = 0.2y_{fp}$ mm and $\epsilon = 0.1y_{fp}$ mm. The non-smooth case is shown by the dashed curve. The smoothing parameter ϵ visually corresponds to about half of the smoothing region as shown in panel (b).

the tyres. Therefore, this damping remains independent of freeplay magnitude and is modelled here as a linear damping of the torsional DoF, taking the form

$$M_{c\psi} = c_\psi \dot{\psi} \ , \tag{16}$$

where the constant c_ψ is given in table 1.

This completes the description of the MLG dynamics, as modelled by the equations of motion (1)–(6), with individual terms as defined in sections II.A–III.

IV. Bifurcation analysis of MLG system

To study the dynamics of the MLG system we perform a bifurcation analysis with the software package AUTO,[17] focusing on the effects of the forward velocity and loading force on the stability of the the system. Throughout this paper we consider the simplest geometric case in which the chord between the MLG attachment points is horizontal and perpendicular to the direction of travel ($\rho = \mu = 0$).

IV.A. Zero freeplay case

We begin by considering the zero freeplay case and construct one-parameter bifurcation diagrams for the velocity V as the principle continuation parameter. These diagrams are shown in figure 7 for loading values of $F_z^* = 0.2$ and $F_z^* = 1$. Solution curves are shaded in accordance with their stability and the point H indicates a point of Hopf bifurcation. These solutions are expressed in terms of their torsional and lateral amplitudes only. This is because for the simplest geometric case ($\rho = \mu = 0$) the longitudinal and axial DoFs

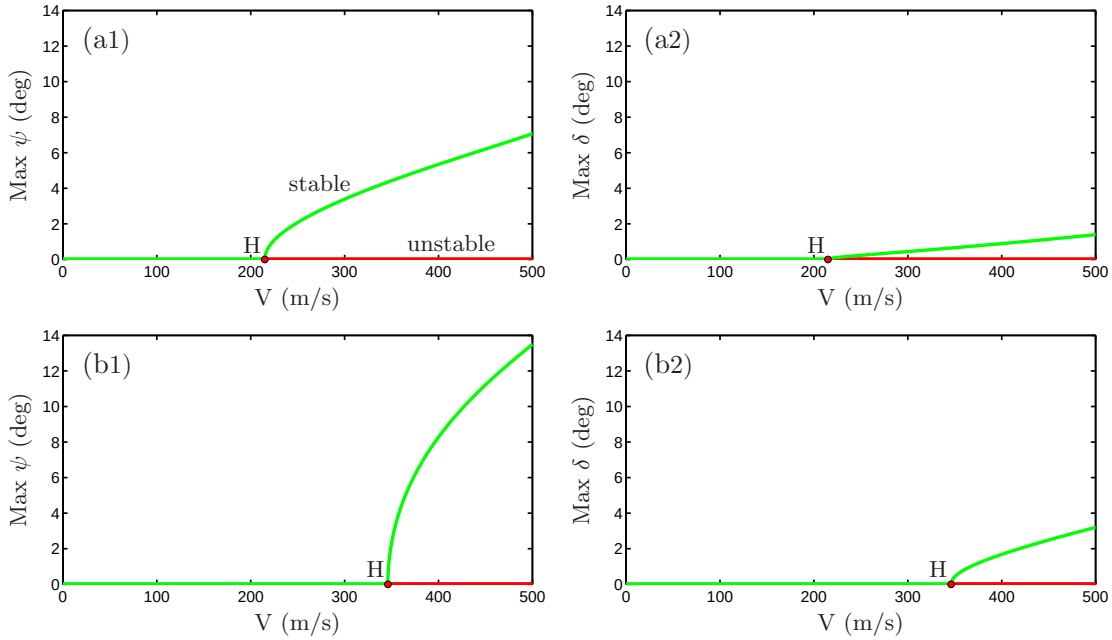

Figure 7. **One-parameter bifurcation diagrams for zero torque link freeplay. Panels (a1) and (a2) show the bifurcation diagrams for a loading force of $F_z^* = 0.2$ expressing solutions in terms of their torsional and lateral amplitudes respectively. Panels (b1) and (b2) show the $F_z^* = 1$ case. Throughout, green/light curves and red/dark curves correspond to stable and unstable solutions, respectively.**

remain uncoupled from the MLG dynamics, passively following oscillation of the torsional and lateral DoFs.[4]

We see that in both cases, the zero amplitude straight-rolling solution is stable for lower velocity values. As V is increased however, the solution loses stability at a super-critical Hopf bifurcation, beyond which the system will experience shimmy oscillations. These shimmy oscillations have a larger torsional than lateral amplitude and hence, we refer to them as torsional shimmy. However, looking at the velocity range shown we note that for both $F_z^* = 0.2$ and $F_z^* = 1$, the velocity above which the MLG system loses stability is far in excess of the realistic operating region for the landing gear of up to 80 m/s. An example of shimmy oscillation within this high-velocity region is shown in figure 8 where we perform a numerical simulation for a forward speed of $V = 300$ m/s and a loading force of $F_z^* = 0.2$ with initial conditions on the unstable solution branch. The resulting time series is shown in terms of its amplitude in the ψ, δ, β and η DoFs and spans a period of 15 seconds. A zoom of the final second of simulation is also shown to the right of each time series to indicate the settled response. In figure 8 we observe the growth of shimmy oscillations, eventually settling to the amplitude indicated by the solution curves of figure 7(a1) and 7(a2); as predicted the torsional DoF constitutes the largest component of these oscillations. We also observe from figure 8 that the longitudinal and axial DoFs β and η show only a weak coupling throughout,

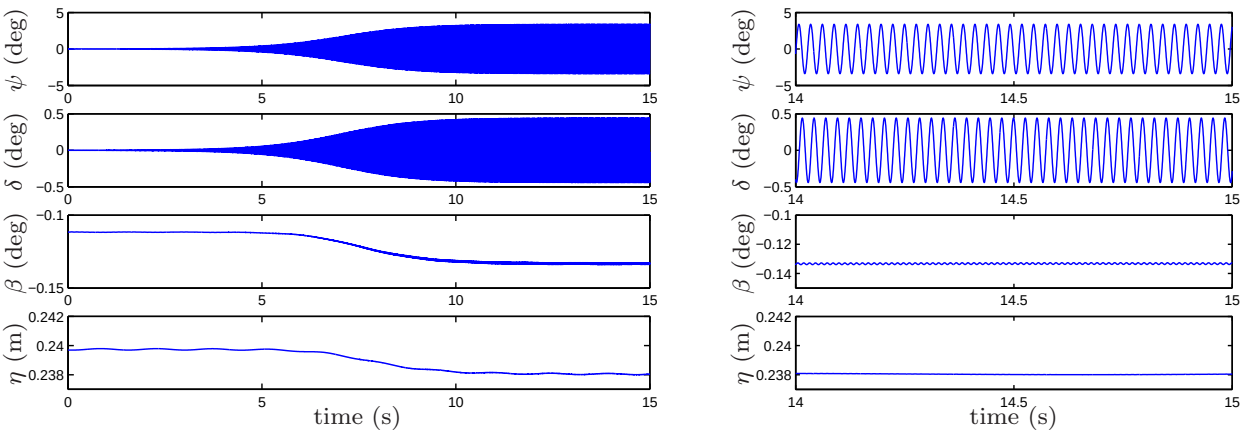

Figure 8. Simulation results in ψ, δ, β and η for $(V, F_z^*) = (300, 0.2)$

oscillating with very small amplitude. However, as the amplitude of oscillation grows we note a reduction in the equilibrium values of β and η, which is a consequence of the increased drag acting on the system at the onset of shimmy.

We note from figure 7 that the critical velocity above which the system experiences shimmy is given by the Hopf bifurcation point H and, moreover, the location of this point varies with the applied load F_z^*. This agrees with the discussions in section II.B highlighting the sensitivity between the MLG parameters and the loading force. We therefore proceed by plotting the Hopf bifurcation point of figure 7 over a range of loading forces. This is achieved by continuing this Hopf bifurcation in the additional parameter F_z^*, yielding the two-parameter bifurcation diagram in the (V, F_z^*)-plane shown in figure 9. We see that the resulting Hopf bifurcation curve bounds a region of stable non-oscillatory behaviour in this plane; however, for higher speeds and loading forces to the right of the curve H the system loses stability and torsional shimmy may be observed in the dynamics. In agreement with the one-parameter diagrams in figure 7, this torsional shimmy only occurs well outside of the typical MLG operating range, which is indicated by the dashed lines. Therefore, despite the existence of a region of instability, one would not expect to observe sustained shimmy oscillation of the MLG for the case shown in figure 9.

IV.B. Non-zero freeplay case

Having established that the MLG remains stable over its operating range for the zero freeplay case, we now explore the effect of a non-zero freeplay at the torque link apex. Figure 10 shows the one-parameter bifurcation diagram for the MLG with ± 1 mm of torque link freeplay. The loading force is fixed at $F_z^* = 1$ and oscillatory solutions are expressed in terms of their

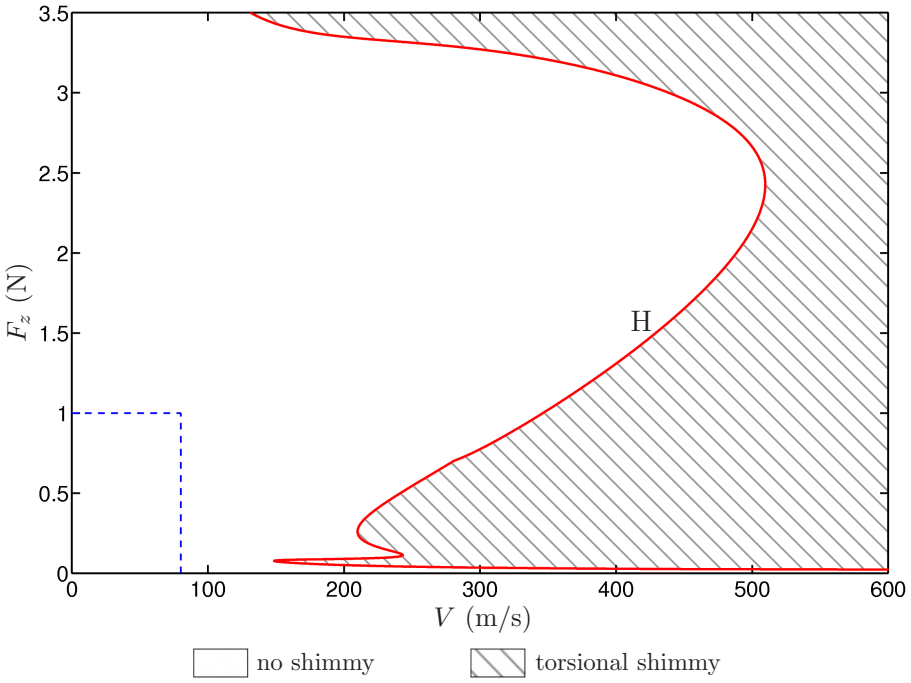

Figure 9. Two-parameter bifurcation diagram for the zero freeplay case.

torsional amplitude in panel (a) and their frequency in panel (b). The zero freeplay solution is given by the dashed curve for reference. Figure 10(a) shows — with the introduction of freeplay — a shift in the Hopf bifurcation point H of figure 7 from $V = 346.1$ m/s to $V = 142.5$ m/s, as well as the creation of a second pair of Hopf bifurcations, also labelled H, at $V = 1.5$ m/s and $V = 28.1$ m/s. This is because, as freeplay is introduced into the MLG, the nature of the system near to the zero-amplitude solution changes, with the torsional stiffness approaching zero as $\epsilon \to 0$. This results in a rapid change of the bifurcation diagram near the zero-amplitude solution; indeed the bifurcation diagram in figure 10(a) differs greatly from the zero freeplay case of figure 7(a1) in terms of the small amplitude behaviour close to the x-axis. For large amplitude responses, away from the zero-amplitude solution, the freeplay region has a much smaller influence on the dynamics, with periodic solutions approaching the zero freeplay case as their amplitudes increase. This may also be observed in figure 10(b), wherein we see the frequency of the stable solution curve approaching the zero freeplay solution with increasing velocity V.

As a consequence of the freeplay, we now see a greater velocity range over which oscillatory solutions exist and, hence, shimmy may be observed; we note that this range now lies within the realistic operating region of the MLG. Furthermore, for $V \in (41.5, 142.5)$ the zero-amplitude solution remains stable, despite the presence of a stable oscillatory solution

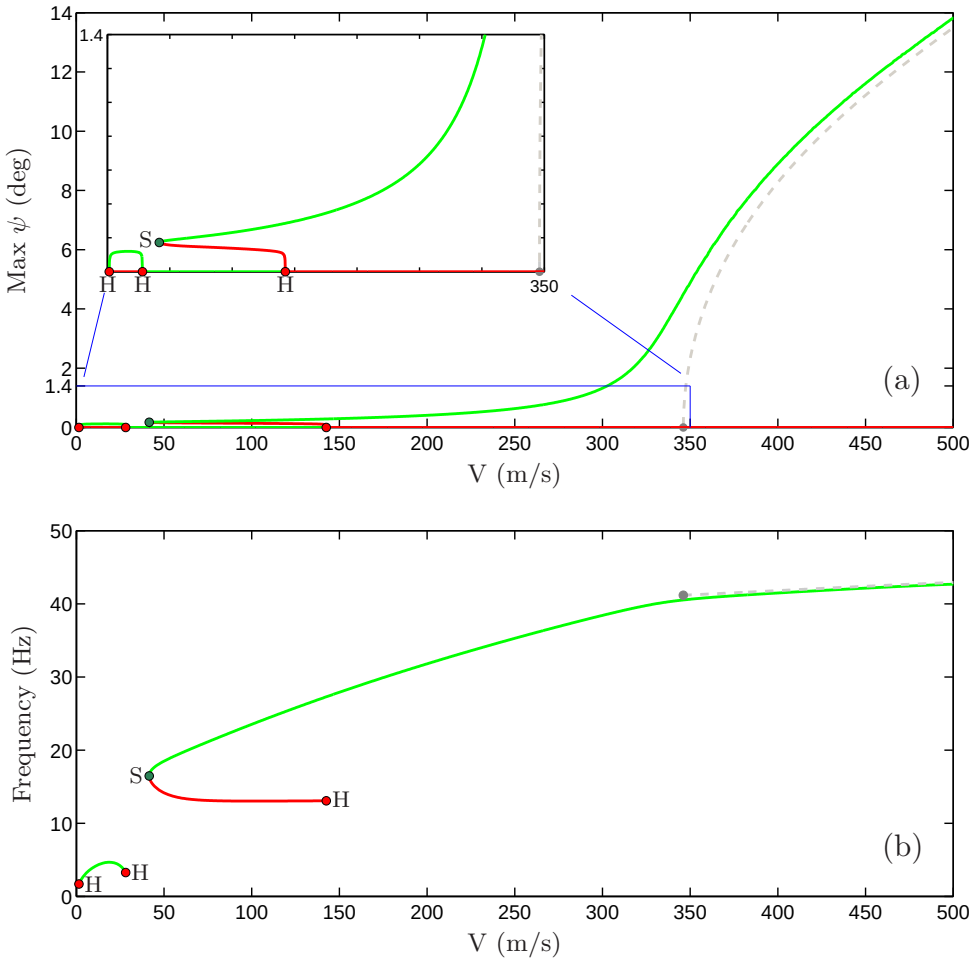

Figure 10. **One-parameter bifurcation diagram for $F_z^* = 1$ and ±1 mm of torque link freeplay. Panel (a) shows the torsional magnitude of solutions (including a zoom of the small ψ-amplitude features) and panel (b) their frequency. The dashed curve indicates the solution branch for the zero freeplay case.**

branch bounded by the new saddle node bifurcation point S in figure 10. Therefore, within this region the MLG may experience both stable and shimmy behaviour with the possibility that — in the presence of perturbing forces — the system may jump between these two behaviours. The two additional Hopf bifurcation points at $V = 1.5$ m/s and $V = 28.1$ m/s connect a second stable periodic solution. Although this solution also indicates torsional shimmy of the MLG, we see from panel (b) that the resulting oscillations are of lower frequency and are 'gentler' in nature, owing to the small amplitude of this solution branch. Hence, each individual periodic orbit lies almost entirely inside the freeplay region, thereby experiencing a lower overall restorative stiffness force and lower frequency of oscillation.[5]

We now proceed as before and continue the bifurcation points observed in figure 10 in the additional parameter F_z^*, producing the two-parameter bifurcation diagram shown in figure 11; regions of oscillation are shaded as indicated in the key. The curve $y_{fp} = 0$ illustrates

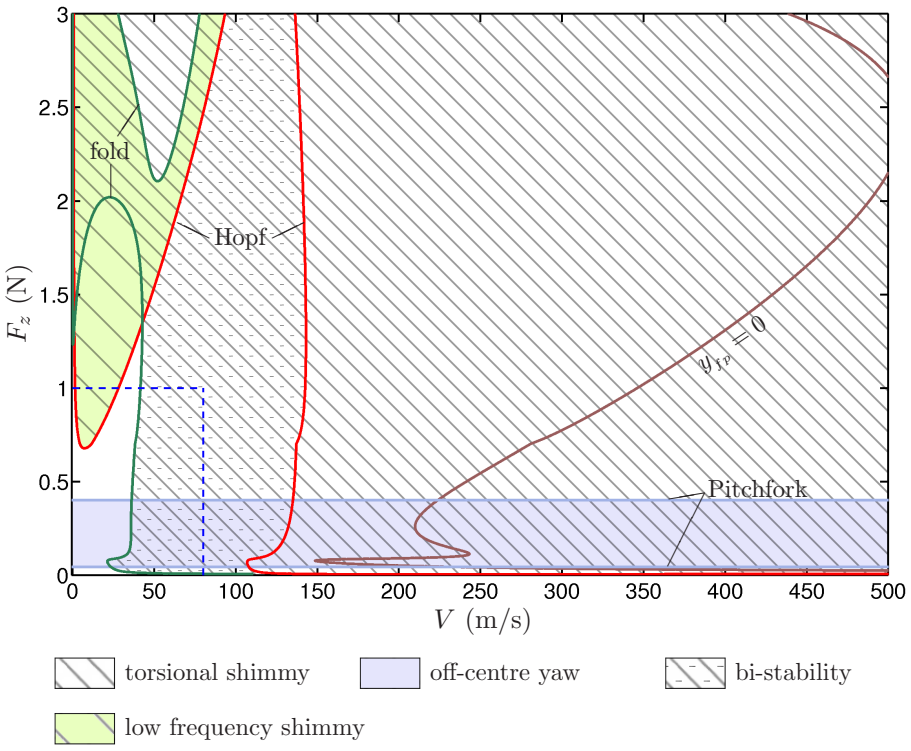

Figure 11. Two-parameter bifurcation diagram for ±1 mm of torque link freeplay.

the Hopf bifurcation curve for the zero freeplay case. We note here that the other two Hopf curves are in fact both part of a single curve that enters and exits the displayed region twice. As freeplay is introduced into the torque links, the Hopf bifurcation curve quickly shifts to take this shape. We also observe the creation of two fold curves, forming part of the stability boundary between regions of shimmy oscillation.

As a result of the addition of torque link freeplay, the total parameter range over which shimmy oscillations may be observed increases substantially. In particular, this behaviour may now be observed over typical operating velocities and vertical loads. Equivalently, the non-shaded region indicating straight-line stability now spans a much smaller parameter range and is bounded by the Hopf and lower fold bifurcation curves. Crossing the Hopf bifurcation curve from this stable region we note a loss in stability of the zero-amplitude solution, and the creation of low frequency oscillations (wide shading). These oscillations have small amplitude, lying mostly inside the torsional freeplay region. However, if we start within the stable region and instead cross the fold bifurcation curve we observe a different type of dynamics. This time the zero-amplitude solution remains stable but there also exists a high-frequency torsional solution. We call this the bi-stable region within which the MLG

may experience either stable or oscillatory dynamics. We note that this second oscillatory solution has a higher amplitude and frequency and, therefore, a much greater power than the first, inflicting a greater stress on the MLG and representing a larger risk of damage to the system. Consequently, the presence of perturbing forces proves especially critical within this linearly stable region, with the right disturbance capable of moving the system between stable straight-rolling and high-frequency shimmy oscillation. Other features of interest include a region of bi-stability to the top left of figure 11 where both low-frequency and high-frequency solutions co-exist. Again, given the right perturbation it is possible to move the response between these two types of solution.

IV.C. Steady non-zero yaw

At the bottom of figure 11 we see a shaded region of off-centre yaw bounded by two pitchfork bifurcation curves. This region is due to the small negative rake angle of the MLG, resulting in the zero-amplitude solution ($\psi = 0$) becoming geometrically unstable; thus, the wheel axle experiences a small destabilising moment. Usually this instability is strongly resisted by the torque link stiffness; however, within the freeplay region this stiffness falls to zero and the destabilising moment is opposed only by the restoring torque produced by the tyres. In fact, there exists a range of loading forces for which this self-aligning torque is insufficient to counter the geometric instability and, therefore, we observe the creation of two pitchfork bifurcation curves. These curves are functions of vertical force only and so appear as horizontal lines in the two-parameter bifurcation diagram. This reflects the assumptions on the tyre model parameters, which vary only with applied loading force, independent of forward velocity.

To illustrate the effect of this region of off-centre yaw, we take F_z^* as a bifurcation parameter to produce the one-parameter bifurcation diagram shown in figure 12. Here V is fixed at 50 m/s and solutions are expressed in terms of their torsional amplitude. Bifurcation points are as labelled, the dot-dash curves indicate non-zero stationary solution branches, and the boundary of torsional freeplay is given by the thicker grey curve. Increasing the loading force from zero we see that at the first pitchfork bifurcation the zero-amplitude solution loses stability and two stationary non-zero solutions are created. Due to the symmetry of the MLG system for $\mu = \rho = 0$ these solutions are symmetric about $\psi = 0$ and quickly grow in amplitude, approaching the boundary of torsional freeplay. However, note that due to the smoothing of the freeplay profile these solutions experience an increasing torsional stiffness as they approach this freeplay boundary and, therefore, they do not reach the grey curves shown. At the second pitchfork bifurcation the self-aligning moment produced by the tyres is once again sufficient to oppose the geometric instability of the MLG

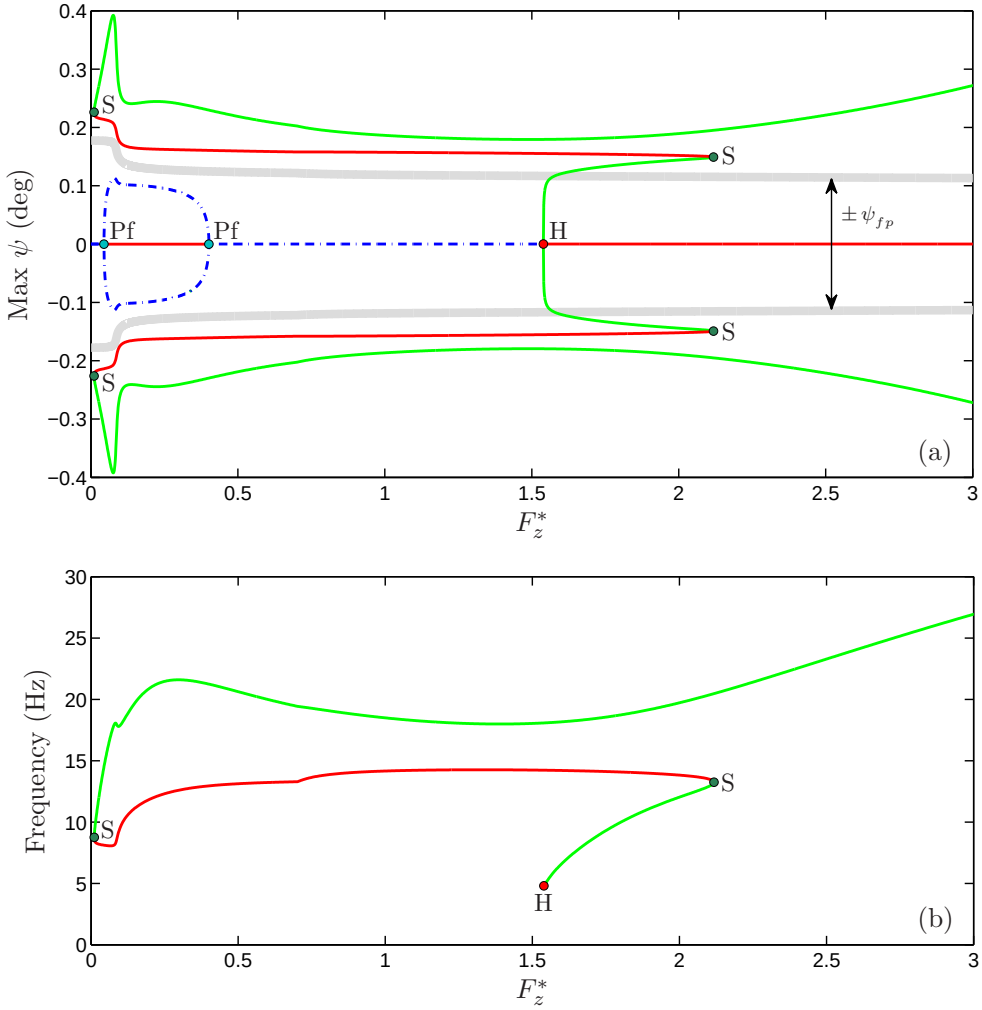

Figure 12. One-parameter diagram for a freeplay of ±1 mm, where F_z^* is the bifurcation parameter and V is fixed at 50 m/s. Solutions are expressed by their torsional amplitudes (a) and frequency (b). The boundary of torsional freeplay is also indicated by the thicker grey curve in panel (a).

and the zero-amplitude solution regains stability. As F_z^* is increased further this solution undergoes a supercritical Hopf bifurcation leading to the creation of a branch of torsional shimmy solutions spanning the entire F_z^* range considered. Panel (b) of figure 12 shows the frequency of oscillation along the solution branch. The branch has stable segments of both low and higher frequency behaviour, reflecting the amplitude of oscillation, and these are separated by an unstable section of the same branch. In addition, we see in panel (a) that for $(V = 50, F_z^* \in (0.01, 1.54))$, this unstable section separates straight-rolling and torsional shimmy oscillations, and we note that this corresponds to the region of bistability shaded in figure 4.8. In particular we see that for $(V = 50, F_z^* \in (0.01, 1.54))$, straight-rolling behaviour is separated from torsional shimmy by the unstable solution branch, and this corresponds to the region of bi-stability shaded in figure 11. It is within this region that the appearance of pitchfork bifurcations proves particularly significant to the dynamics of the MLG. Here,

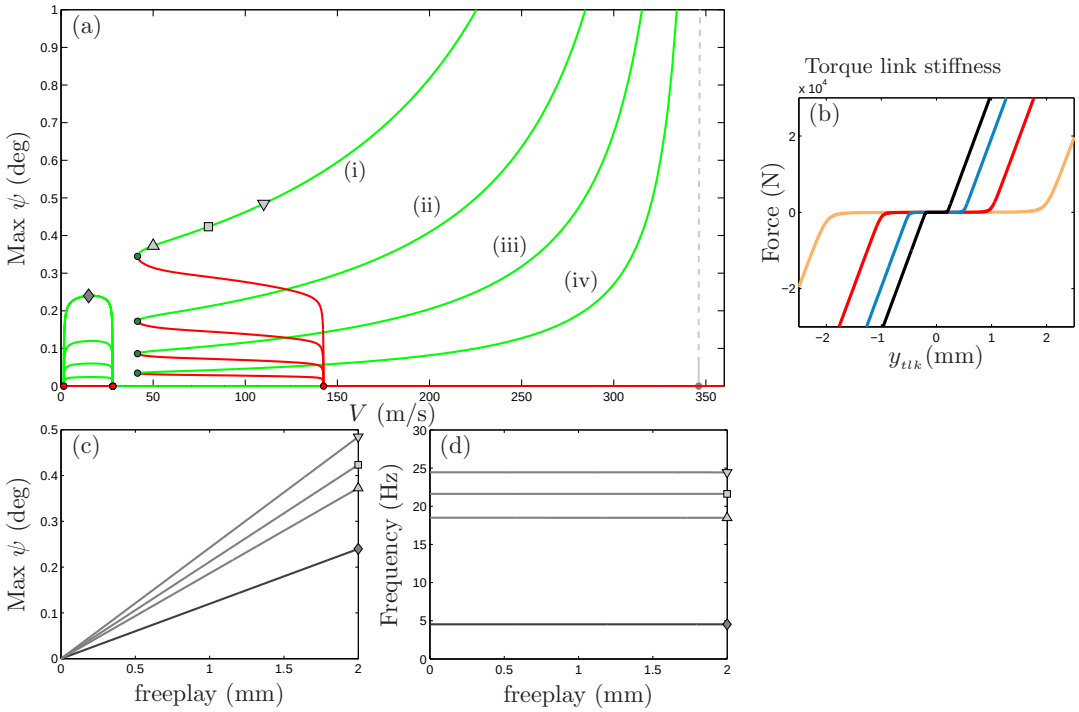

Figure 13. Variation of torsional shimmy amplitude with freeplay magnitude for the case $\epsilon = y_{fp} \times 10^{-1}$ mm; torque link freeplays of y_{fp} = 0.2 mm (i), 0.5 mm (ii), 1 mm (iii) and 2 mm (iv) are considered.

relatively small perturbations to the system from the non-zero stationary solutions are sufficient to set up transient oscillations in the dynamics that eventually settle into self-sustained torsional shimmy oscillations.

IV.D. Quantitative effect of torque link freeplay

As it was demonstrated that torque link freeplay destabilises the small amplitude response of the MLG system, we now wish to gauge the quantitative influence of freeplay magnitude on the observed shimmy oscillations. We therefore consider the one-parameter bifurcation diagram of figure 10 for $F_z^* = 1$ over a variety of torque link freeplay magnitudes. As discussed in section III, this variation is modelled in two ways: by maintaining a fixed scaled freeplay profile $\{(\epsilon, y_{fp}) : \epsilon/y_{fp} = const\}$, or by keeping a smoothing region of constant size $\{(\epsilon, y_{fp}) : \epsilon = const,\ y_{fp} \in \Re^+\}$.

IV.D.1. Fixed scaled freeplay profile

Figure 13 shows the results for $\epsilon/y_{fp} = const$. Keeping the loading force fixed at $F_z^* = 1$, we show in panel (a) simultaneously the one-parameter bifurcation curves for freeplay values y_{fp} of 0.2, 0.5, 1 and 2 mm producing solutions of increasing amplitude, respectively. For each case we also plot the corresponding torque link stiffness profile of $(M_{k\psi}/r_{tlk})$ vs (y_{tlk}) in panel (b); see equation (15). These profiles become less 'sharp' with a more gradual

change in curvature along their length, as the magnitude of torque link freeplay is increased. However, when rescaled such that $x^* = x/y_{_{fp}}$, $y^* = y/k_{_{tlk}}$ and plotted together, as shown in figure 15(a), the same scaled stiffness profile is maintained over all cases. This type of freeplay variation produces a pure scaling of the solution curves in panel (a), and we see that the forward velocities at which the bifurcation points occur remain fixed.

To gauge the rate at which the amplitude of these shimmy oscillations grows with increasing freeplay we consider four stable periodic orbits for $V = 15, 50, 80, 110$ m/s and plot their torsional magnitude as the torque link freeplay is varied. This is shown in figure 13(c), where the amplitude of these oscillations — created with the introduction of freeplay — shows an overall linear scaling with respect to freeplay magnitude. In figure 13(d) we also note that the frequency of these oscillations remains largely independent of torque link freeplay. Therefore, from these results we infer that, providing the same scaled freeplay profile is maintained, the parameter subsets spanned by the bifurcation curves and shaded regions of figure 11, as well as their frequency characteristics, will remain effectively unchanged as the freeplay magnitude is varied. Only the amplitude of shimmy oscillations will change, and these scale linearly with torque link freeplay.

IV.D.2. Constant size smoothing region

Results for a constant smoothing region, inferring constant ϵ are shown in figure 14; again $F_z^* = 1$ throughout as $y_{_{fp}}$ is varied. Panels (a)–(f) correspond to torque link freeplays $y_{_{fp}}$ of 0.05, 0.098, 0.11, 0.15, 0.35 and 1.0 mm, respectively; for each case the corresponding stiffness profile is shown to the right of the one-parameter bifurcation diagram. The smoothness of the transition as the torque links come into contact remains constant for each profile as a consequence of the constant ϵ condition. These profiles are again rescaled and are shown together in figure 15(b) and we see that, unlike the previous case $\epsilon/y_{_{fp}} = const$, the rescaled curves do not coincide for different $y_{_{fp}}$. As before, we focus on four periodic orbits for V of 15, 50, 80 and 110 m/s, which we continue in $y_{_{fp}}$. Resulting projections of their torsional amplitude and frequency are shown in panels (g) and (h) of figure 14, respectively. The dot-dash curves in panel (h) indicate the Hopf bifurcation curves from which the periodic orbits bifurcate.

Figure 14(g) shows that the amplitude of oscillation again increases with greater torque link freeplay; however, now these oscillations do not exist for all values of freeplay. Instead, for each curve there exists a freeplay threshold beyond which oscillatory solutions are created. These solutions quickly grow in amplitude, eventually settling to the trends observed for the linear scaling case in figure 13; again the frequency of oscillation along these solution

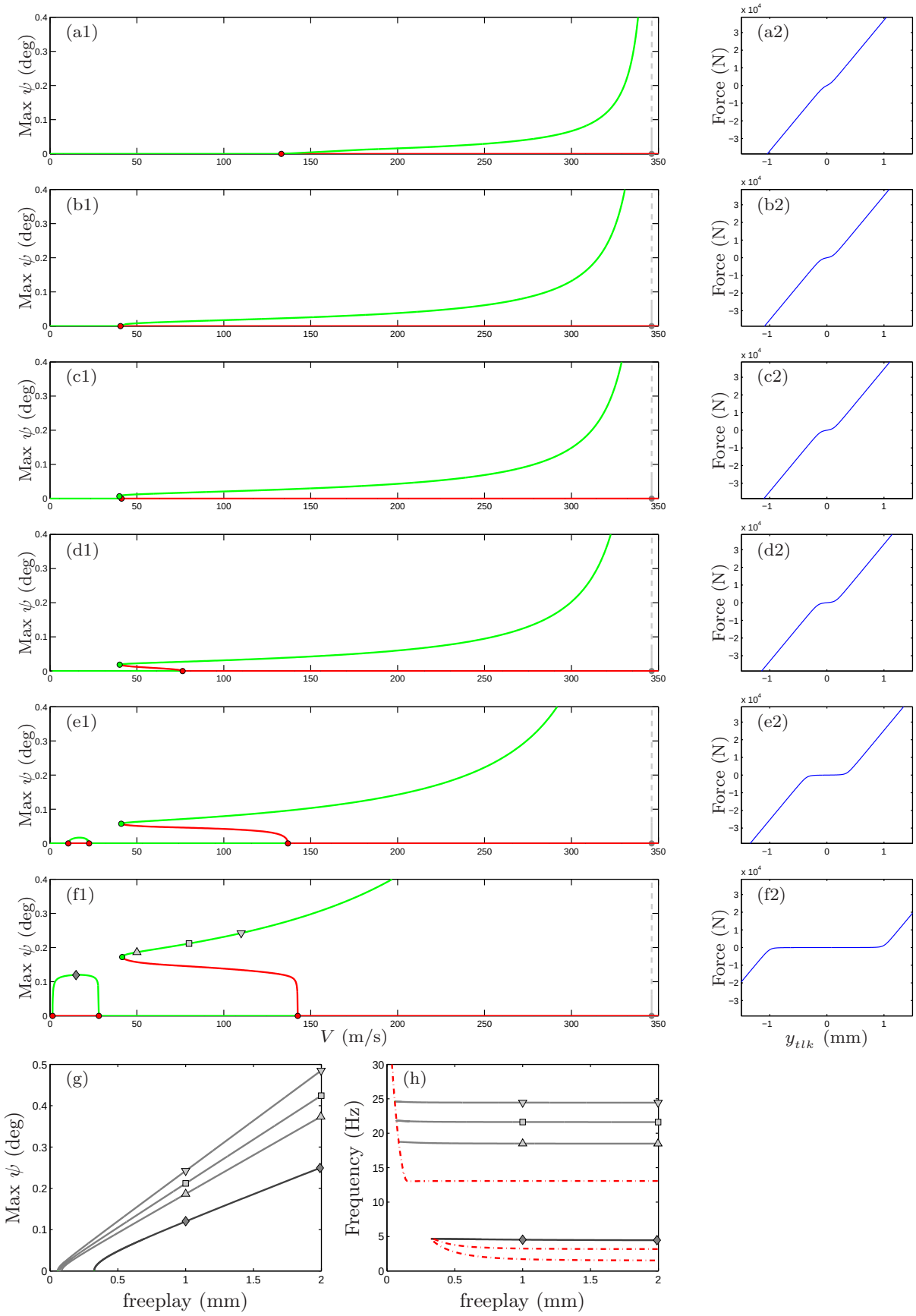

Figure 14. Variation of torsional shimmy amplitude with freeplay magnitude for the case of fixed $\epsilon = 0.1$ mm.

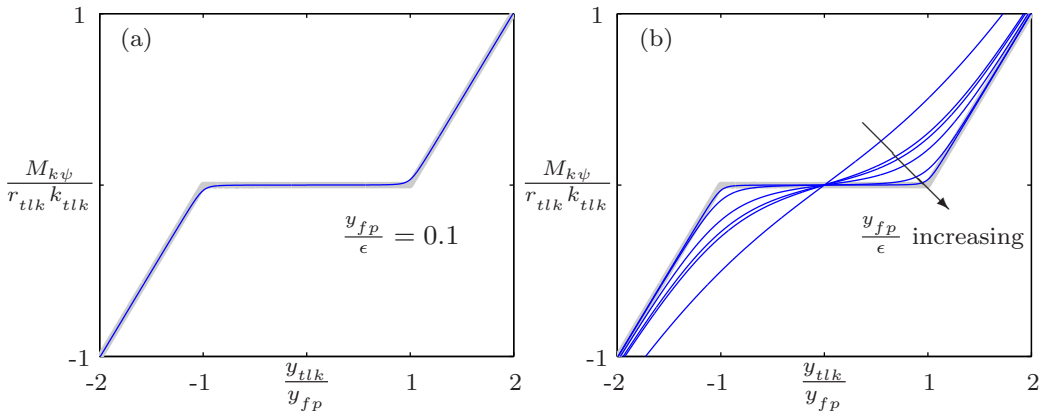

Figure 15. Rescaled plots of torque link force vs. deflection for the two freeplay variation methods. Panel (a) shows the rescaled curves of figure 13 for the fixed scaled freeplay profile discussed in section IV.D.1. Panel (b) shows the curves of figure 14 for a constant size smoothing region; section IV.D.2.

curves remains largely constant; see panel (h) of figure 14. We therefore note that for this case, where we allow the scaled freeplay profile to vary (15(b)), the presence and location of the bifurcation points now depends on the magnitude of torque link freeplay. This represents a key difference from the results of section IV.D.1.

IV.E. Allowable freeplay threshold

Figure 16 shows the oscillatory solutions for the cases $\epsilon/y_{fp} = const$ (a) and $\epsilon = const$ (b), plotted as surfaces parameterised by (V, y_{fp}). As in the previous sections we express the amplitude of oscillations on these surfaces in terms of their torsional amplitude ψ. The one-parameter bifurcation diagrams of figures 13 and 14 are slices through these surfaces for constant y_{fp}, and example cross sections are highlighted in both panels of figure 16. Curves of Hopf and saddle node bifurcations are shown as dot-dash curves. We saw that for $\epsilon/y_{fp} = const$ the location of the bifurcation points remain independent of freeplay magnitude and, hence, these bifurcation curves appear as straight lines with constant V in figure 16(a). In panel (b) we observe that this is not the case, with bifurcation curves depending on V and y_{fp}. Consequently, there exist values of y_{fp} for which the zero-amplitude solution remains stable over a range of typical operating speeds.

To illustrate this point we consider an absolute upper limit for the MLG forward velocity of 120 m/s and in figure 16(b) highlight two rectangular regions R1 and R2 over which the zero-amplitude solution is stable up to this limit. Together these regions show that for a loading force of $F_z^* = 1$ and a smoothing region of size $\epsilon = 0.1$ mm the landing gear may remain stable up to forward speeds of $V = 120$ m/s, providing the magnitude of torque

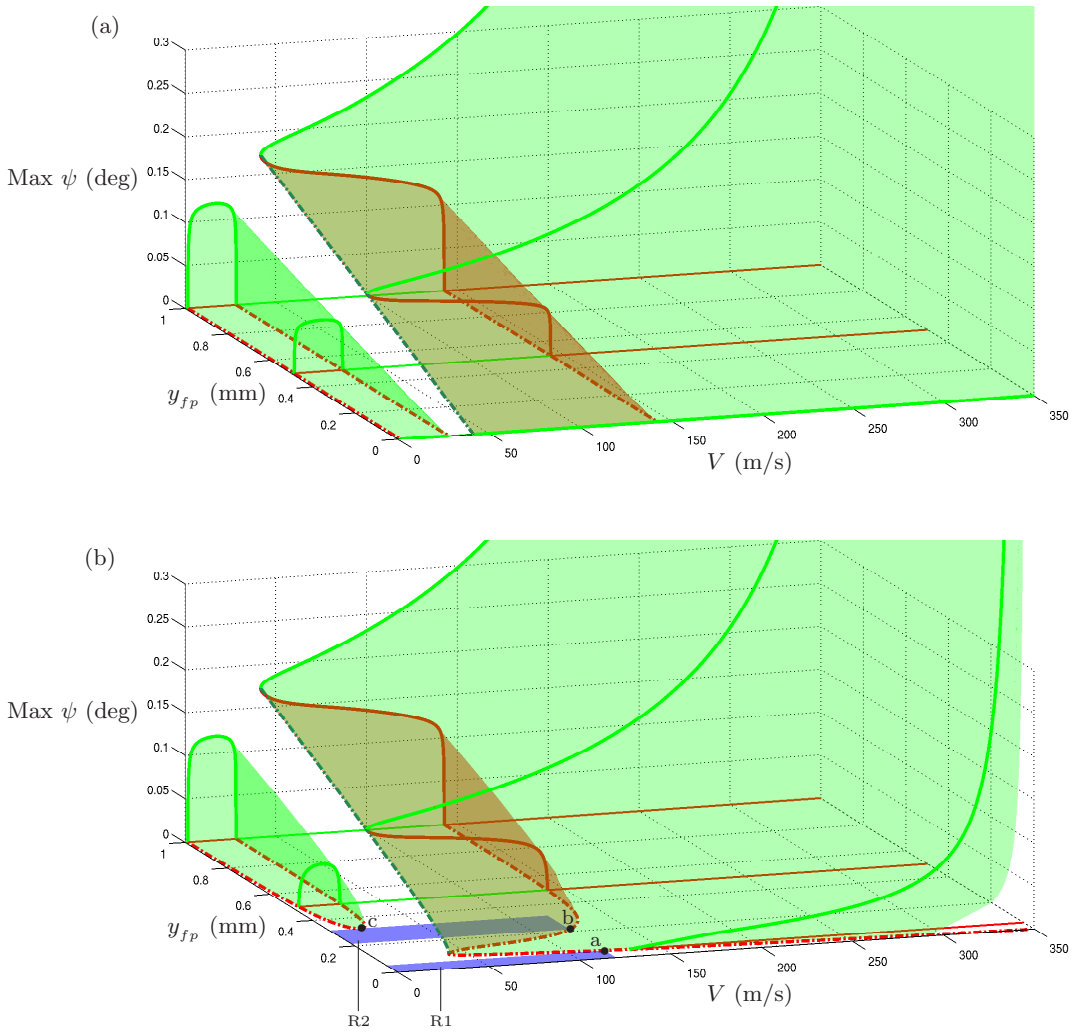

Figure 16. Surface plots of oscillatory solutions as forward velocity V and freeplay magnitude y_{fp} are varied, where the vertical force is fixed at $F_z^* = 1$. Panels (a) is for constant $\epsilon/y_{fp} = 0.1$ and panel (b) for constant $\epsilon = 0.1$ mm.

link freeplay remains in the range $y_{fp} \in (0, 0.055) \cup (0.22, 0.32)$. However, we may further generalise these results by considering the points discussed earlier in sections IV.D.1 and IV.D.2. We recall that for constant (y_{fp}/ϵ) bifurcation points remain fixed, occurring at the same parameter values. This result may be extended to figure 16(b) whereby we note that, providing the y-axis is scaled to span the same range of (y_{fp}/ϵ), the orthogonal projection of the bifurcation curves onto the (V, y_{fp})-plane will remain unchanged and only the height (maximal amplitude of ψ) of the solution surfaces will change.

This insensitivity with respect to the quantity (y_{fp}/ϵ) allows the planar projection of figure 16(b) in (V, y_{fp}) to be plotted as shown in figure 17. This time the rectangular regions represent ranges of (y_{fp}/ϵ), prescribing an allowable set of freeplay 'shapes' depending on y_{fp} and ϵ, rather than simply a maximal freeplay width. These regions are bounded by three

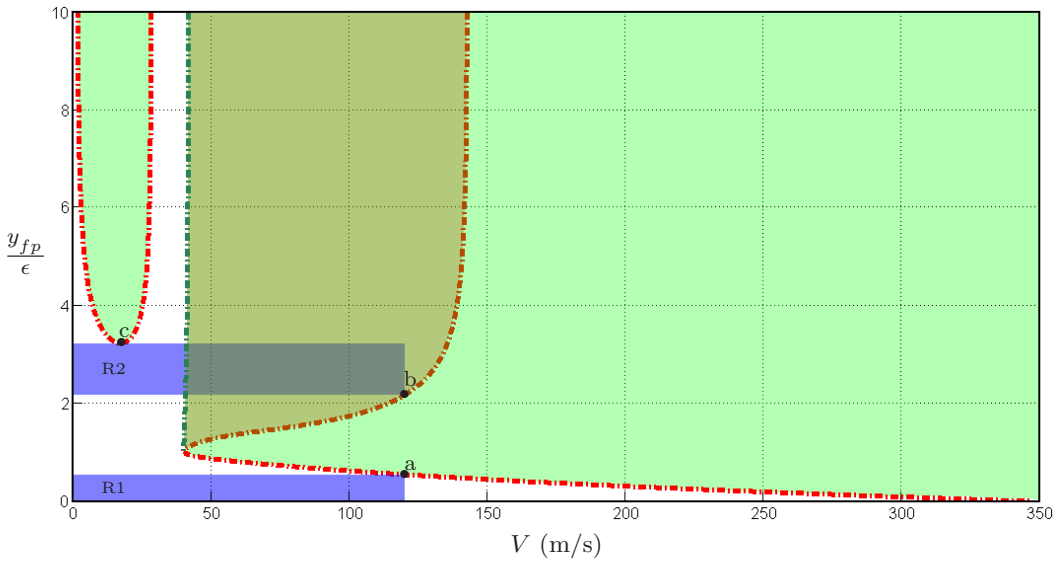

Figure 17. Projection of the bifurcation curves of figure 16(b) onto the plane $(V, y_{fp}/\epsilon)$**.**

points a, b and c as indicated and, with the package AUTO, we may continue these points in the loading parameter F_z^*. Figure 18 shows projections of the resulting three curves in the (y_{fp},F_z^*)-plane. These curves divide this parameter plane into regions of different behaviour over the velocity range $V \in [0, 120]$ m/s. There are two regions where the straight-rolling solution is stable, which are labelled R1 and R2; a lightly shaded region — reached by crossing the curve c from R2 — in which the system may experience 'gentle' oscillations, and an unshaded region bound by the curves a and b, where high-frequency shimmy may be observed.

From the diagram in figure 17 we are able to determine the range of allowable torque link freeplays ensuring stability over $V \in [0, 120]$. This is equivalent to finding a rectangular operational envelope in (y_{fp}, F_z^*) that lies entirely within the set $\{\mathrm{R1} \cup \mathrm{R2}\}$. However, looking back to figure 16 one notes that above R2 there also exists a stable oscillatory branch for high forward speeds, where the system may be perturbed from straight-rolling to oscillatory behaviour. Therefore, R2 represents the less desirable of the two stable regions and so, in practice, one would wish the operating conditions of the system to remain in R1. We now impose a second stability condition on the system, requiring that the MLG system is to remain stable over a suitable range of loading forces as well as forward speeds. We again choose a conservative estimate, this time for the maximum loading experienced by the landing gear; specifically we require stability up to a loading force of $F_z^* = 2$. To meet this stability condition we therefore highlight in figure 18 a maximal envelope covering R1 for loading forces in the range $F_z^* \in [0, 2]$.

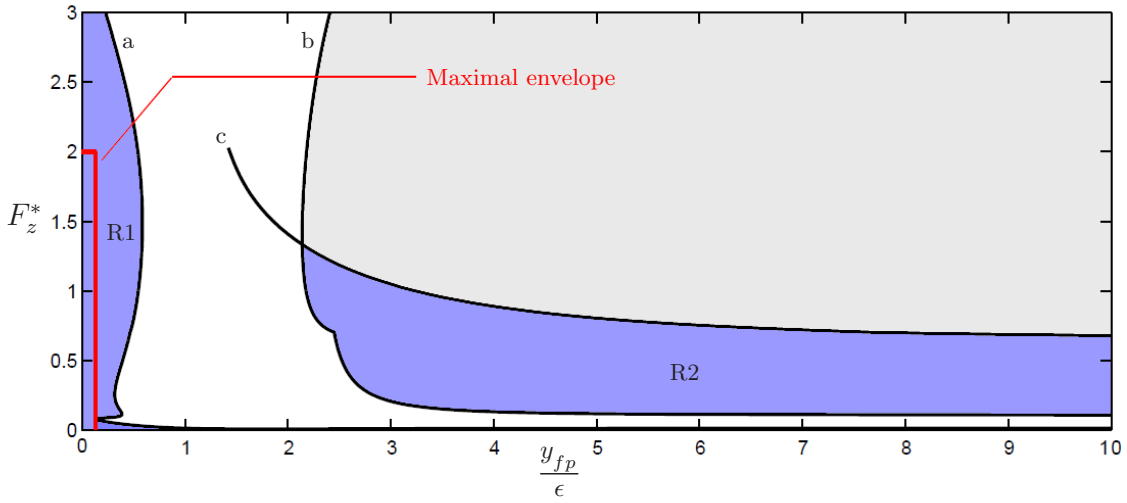

Figure 18. Regions of stability in the $(y_{fp}/\epsilon, F_z^*)$-plane.

We see here that to ensure the absence of shimmy oscillations over the operating regime requires a freeplay quantity (y_{fp}/ϵ) significantly smaller than the value of 10 considered in section IV.B; namely one must satisfy the condition

$$\frac{y_{fp}}{\epsilon} < 0.13\,, \tag{17}$$

which defines the range of permissible freeplay profiles. This range is indicated in figure 19: a given freeplay profile satisfies condition (17) if, when rescaled, it lies entirely within the shaded region. Looking back at figure 18 we note that increasing the freeplay quantity (y_{fp}/ϵ) beyond this value will result in shimmy oscillations appearing for low F_z^*. Therefore, beyond this maximal freeplay threshold one would expect shimmy oscillations to appear first under light landing scenarios or just prior to take off, when loading forces are minimal.

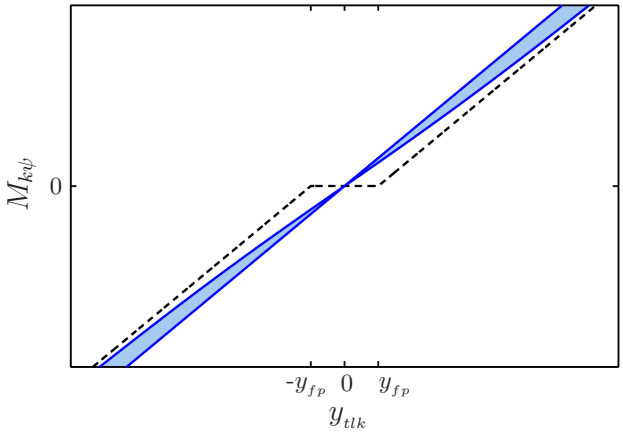

Figure 19. Shaded region indicating the range of allowable scaled freeplay profiles satisfying the condition $y_{fp} < 0.13\epsilon$. The dashed curve indicates the limit $\epsilon \to \infty$

V. Conclusions

In this study we employed numerical bifurcation techniques to analyse a model of a nonlinear dual-wheel main landing gear (MLG) with freeplay at the torque link apex. By continuing key bifurcation points in both the forward velocity V and the vertical loading F_z^* we were able to divide the (V, F_z^*)-plane into regions of different dynamical behaviour. For zero freeplay this highlighted the presence of torsional shimmy oscillations in the dynamics of the system, but only well beyond the range of likely operating conditions. This changed with the introduction of freeplay to the system which permitted the appearance of shimmy oscillations within the typical envelope of MLG operating conditions. The variety of observable dynamics also increased, with the appearance of regions of low-frequency and high-frequency shimmy oscillations. We also note that the amplitude of oscillation in these regions varied with freeplay magnitude and two methods of freeplay variation were investigated. The first, in which the smoothing region was held as a constant proportion of freeplay magnitude (thus maintaining a constant scaled freeplay profile), produced a linear scaling of the periodic solution amplitudes. Furthermore, this scaling did not affect the location of bifurcation points or the frequency of oscillations, and consequently the corresponding two-parameter bifurcation diagram was preserved with the regions of observed shimmy remaining unchanged. This was not the case for the second method of scaling, where the size of the smoothing region was held constant regardless of freeplay magnitude. This represents the more realistic of the two scaling methods, where the constant smoothing region may represent the physical presence of material (dirt, grease, etc.) at the torque link apex. Again, under this type of variation, the amplitude of shimmy oscillations increased with freeplay magnitude; however their scaling was no longer linear for small amplitudes. The location of bifurcation points in the system also proved sensitive to the magnitude of torque link freeplay for this case. Consequently, we were able to identify freeplay ranges in which the MLG system remains stable over an acceptable operational envelope. Furthermore, we found that in fact, when considered along with variation of the smoothing region ϵ, the condition of stability imposed a condition on the allowable shape of the freeplay stiffness profile with sufficiently smooth profiles ensuring stability over the prescribed operating region. For freeplay 'shapes' just outside this stability condition the results suggested the appearance of shimmy oscillations given lightly loaded, high-velocity conditions.

We note that these findings may be used to draw more general conclusions regarding the investigation of torque link freeplay. For this study we chose to represent freeplay as a region of low stiffness using inverse tangent functions to approximate the smooth transition to contact. However, for any generic torque link stiffness model, expressed as a function of torque

link deflection alone, one would expect the same invariance of the bifurcation curves to hold when maintaining a constant scaled profile. Therefore, one may apply a similar methodology to a broad family of different freeplay representations, using continuation methods to specify conditions that satisfy a given desired stability criterion.

Throughout the study we considered the effect of a variable loading force and this influenced a number of parameters in the MLG model, including modal inertias, gear stiffness and torsional freeplay. The tyre dynamics were particularly sensitive in this respect and we observed a range of loading forces for the non-zero freeplay case over which the self-aligning moment produced by the tyre dynamics was insufficient to oppose the geometric instability created by the negative rake angle of the system. This resulted in a stationary solution of non-zero yaw that, when occurring within the region of linearly stable shimmy oscillations, reduced the threshold between non-oscillatory and shimmy behaviour. This, increased the sensitivity of the system to external perturbation and thus illustrated the possible influence of load dependent parameters on the MLG dynamics. This result highlights the importance of considering relevant nonlinearities in the MLG system and demonstrates the role that nonlinear analysis techniques can play in analysing their effect on the dynamics.

With regards to future work we remark that our previous study results[4] indicate strongly that the complexity of the observed dynamics increases considerably with a change in side-stay orientation. This orientation is varied in the model simply by assigning (non-zero) values to the μ and ρ model parameters. Thus, a natural extension to the analysis presented here would be the investigation of variations of these side-stay angles. There are also a number of additional effects that could be modelled. For example, the presence of Coulomb friction has been found to be an important factor in the development of shimmy in previous studies.[7,16] Its inclusion could present an interesting extension to the current work, as the friction force produced between the oleo piston and shock strut will produce a restorative force even within the region of torsional freeplay. Therefore it may prove to have a significant effect alongside the freeplay phenomenon detailed in this paper.

Acknowledgements

The authors thank Phanikrishna Thota and Duncan Pattrick (Airbus UK) for useful discussions. This research is supported by a Knowledge Transfer Network (KTN) Mathematics CASE Award from the Engineering and Physical Sciences Research Council (EPSRC) in collaboration with Airbus in the UK.

References

[1]Civil Aviation Accident and Incident Investigation Commission (CIAIAC). Accident of aircraft Fokker MK-100, registration I-ALPL, at Barcelona Airport (Barcelona), on 7 November 1999. Technical Report A-068/1999, 2003. `http://www.fomento.es`.

[2]P. Thota, B. Krauskopf, and M. Lowenberg. Interaction of torsion and lateral bending in aircraft nose landing gear shimmy. *Nonlinear Dynamics*, 57(3):455–467, 2009.

[3]I. Besselink. *Shimmy of aircraft main landing gears*. PhD thesis, Delft University of Technology, 2000.

[4]C. Howcroft, B. Krauskopf, M. Lowenberg, and S. Neild. Influence of variable side-stay geometry on the shimmy dynamics of an aircraft dual wheel main landing gear, 2013. *SIAM Journal on Applied Dynamical Systems* (to appear).

[5]N. Sura and S. Suryanarayan. Lateral response of nonlinear nose-wheel landing gear models with torsional free play. *Journal of Aircraft*, 44(6):1991–1997, 2007.

[6]B. Sateesh and D. Maiti. Non-linear analysis of a typical nose landing gear model with torsional freeplay. In *Proc. IMechE Part G: J. Aerospace Engineering*, volume 223, pages 627–641, 2009.

[7]P. Woerner and O. Noel. Influence of nonlinearity on the shimmy behaviour of landing gear. *AGARD-R-800*, 1995.

[8]P. Thota, B. Krauskopf, and M. Lowenberg. Multi-parameter bifurcation study of shimmy oscillations in a dual-wheel aircraft nose landing gear. *Nonlinear Dynamics*, 70(2):1675–1688, 2012.

[9]B. von Schlippe and R. Dietrich. Shimmying of a pneumatic wheel. Technical report, NACA TM 1365, 1941.

[10]P. Thota, B. Krauskopf, and M. Lowenberg. Nonlinear analysis of the influence of tire inflation pressure on nose landing gear shimmy. *Journal of Aircraft*, 47(5):1697–1706, 2010.

[11]R. Daugherty. A study of the mechanical properties of modern radial aircraft tires. Technical report, NASA/TM-2003-212415, Langley Research Center, Hampton, Virginia, 2003.

[12]R. Smiley and W. Horne. Mechanical properties of pneumatic tires with special reference to modern aircraft tires. Technical report, NACA TN 4110, Langley Aeronautical Laboratory, Langley Field, Va., 1958.

[13]S. Clark, editor. *Mechanics of pneumatic tires*, volume 122. NBS Monograph, University of Michigan, 1971.

[14]H. Pacejka and E. Bakker. The magic formula tyre model. *Vehicle System Dynamics*, 21(1):1–18, 1992.

[15]E. Bakker, L. Nyborg, and H. Pacejka. Tyre modelling for use in vehicle dynamics studies. Technical Report 870421, Society of Automotive Engineers, Inc., 1987.

[16]J. Baumann. A nonlinear model for landing gear shimmy with applications to the McDonnell Douglas F/A-18A. *AGARD-R-800*, 1996.

[17]E. Doedel, with major contributions from A. Champneys, T. Fairgrieve, Yu. Kuznetsov, B. Oldeman, R. Paffenroth, B. Sandstede, X. Wang, and C. Zhang. Auto-07P: Continuation and bifurcation software for ordinary differential equations, 2008. available at `http://cmvl.cs.concordia.ca/`.